ADVANCED MATERIALS

Supporting Information

for *Adv. Mater.*, DOI: 10.1002/adma.201807658

MXenes for Plasmonic Photodetection

*Dhinesh Babu Velusamy, Jehad K. El-Demellawi, Ahmed M. El-Zohry, Andrea Giugni, Sergei Lopatin, Mohamed N. Hedhili, Ahmed E. Mansour, Enzo Di Fabrizio, Omar F. Mohammed, and Husam N. Alshareef**

Supporting Information

MXenes for Plasmonic Photodetection

*Dhinesh Babu Velusamy[+], Jehad K. El-Demellawi[+], Ahmed M. El-Zohry, Andrea Giugni, Sergei Lopatin, Mohamed N. Hedhili, Ahmed E. Mansour, Enzo Di Fabrizio, Omar F. Mohammed, Husam N. Alshareef **

[+] *These authors contributed equally to this work.*

Dr. D. B. Velusamy, J. K. El-Demellawi, Dr. A. M. El-Zohry, Dr. A. Giugni, Dr. A. E. Mansour, Prof. E. Fabrizio, Prof. O. F. Mohammed, Prof. H. N. Alshareef
Physical Sciences and Engineering Division, King Abdullah University of Science and Technology (KAUST), Thuwal, Kingdom of Saudi Arabia
E-mail: husam.alshareef@kaust.edu.sa

Dr. S. Lopatin, Dr. Mohamed N. Hedhili
Core Labs, King Abdullah University of Science and Technology (KAUST), Thuwal, Kingdom of Saudi Arabia

EXPERIMENTAL SECTION

Synthesis of 2D Mo_2CT_x

Powders of Mo_2Ga_2C MAX phase were synthesized by a solid liquid reaction of Mo_2C and Ga.[1] To synthesize Mo_2CT_x, 2g of Mo_2Ga_2C MAX powder was immersed into 20 ml of 47-51% hydrofluoric acid (HF, Sigma-Aldrich). The precursor carbides were slowly added into acidic solutions, which were cooled by an ice-bath to minimize localized heating. The mixtures were then stirred with a magnetic Teflon stir bar at room temperature for 168 h (7 days). Following the HF treatment, the acidic suspensions of Mo_2CT_x were washed using cold deionized water (~ 7 ^oC), in consecutive rounds of centrifugation and decanting, until a pH of 6-7 was reached. After discarding the supernatant solution, the solid sediment was kept under vacuum overnight for drying at room temperature. 1g of dried multilayer Mo_2CT_x MXene powder was further re-dispersed into 10 ml of 54-56% tetrabutylammonium hydroxide (TBAOH, Sigma-Aldrich) solution for intercalation, and stirred for 4 h at room temperature. The resulting mixtures were washed three times, and sediments were re-dispersed into cold deionized water followed by ultra-sonication for an hour. The mixtures were later centrifuged at 3500 rpm for 10 minutes. The resulting supernatants were carefully collected and the dispersions were used for the thin film fabrication.

Synthesis of other 2D MXenes

The Ti_3AlC_2 and Ti_2AlC MAX powder were commercially procured (from Carbon-Ukraine ltd. particle size < 40 µm, and from Maxthal 211, Kanthal, Sweden, -325 mesh, respectively). V_2AlC and Nb_2AlC MAX powders were synthesized following previous reports.[2,3] To synthesize $Ti_3C_2T_x$, Nb_2CT_x, T_2CT_x and V_2CT_x MXenes, 2g of Ti_3AlC_2, V_2AlC, Nb_2AlC and Ti_2AlC MAX powders were, respectively, immersed into 20 ml of 47-51% hydrofluoric acid (HF, Sigma-Aldrich), and into 20 ml of 10% HF for the latter MXene. The MAX powders were slowly added into the acidic solutions, which were cooled by an ice-bath to minimize the localized heating. The mixtures were then stirred with a magnetic Teflon stir bar at room

temperature (and 40 °C for $Ti_3C_2T_x$) for 20 h, 160 h, 96 h and 10 h, respectively. As in the case of Mo_2CT_x, following the HF treatment, the resulting suspensions of the other MXenes were washed using cold deionized water, in consecutive rounds of centrifugation and decanting, until a pH of 6-7 was reached. After discarding the supernatant solution, the solid sediments were kept under vacuum overnight for drying at room temperature. The dried multilayer MXene powders were delaminated following the same procedure used for Mo_2CT_x.

Thin Film Photodetector Fabrication

To fabricate the devices, the desired amount of delaminated 2D Mo_2CT_x MXene powders were dispersed in DI water with gentle bath sonication for 1h, then filtered under vacuum onto a nylon membrane filter paper with a pore size of 200 nm and a diameter of 25 mm. The resulting film was dried in a vacuum oven at 80 °C for 4 h. Au electrodes with thicknesses of 50 nm were deposited onto a Mo_2CT_x thin film by e-beam evaporation under a vacuum of 10^{-6} torr using a patterned shadow mask. The length and width of the channels were 70 μm and 1 mm, respectively.

Characterizations

Surface morphologies were observed using a field emission scanning electron microscope (FE-SEM) (Nova Nano 630, FEI, USA). Steady-state UV-Visible-NIR absorption spectra (190-1200 nm) for liquid samples were obtained using a Cary 5000 UV-VIS-NIR spectrometer (Varian Inc.). As for films, UV-Vis-NIR diffuse reflectance spectra were collected using a JASCO model V-670 spectrometer. The reflectance spectra were recorded over the range of 190-1500 nm using halogen and deuterium lamps as the light sources. The reflectance were transformed into absorption coefficient (α) using the Kubelka-Munk function. A baseline correction was applied before obtaining either of the two measurements; absorption and reflectance. X-ray diffraction (XRD) analysis was conducted using a powder X-ray

diffractometer (Bruker D8 Advance, Cu Kα radiation) with scanning rate of 0.02°/step and 0.5 s/step in the range 2θ angles of 3° - 70°.

XPS studies were carried out in a Kratos Axis Supra DLD spectrometer equipped with a monochromatic Al Kα x-ray source (hν=1486.6 eV) operating at 150 W, a multichannel plate and delay line detector under a vacuum of 1×10^{-9} mbar. The survey and high-resolution spectra were collected at fixed analyzer pass energies of 160 eV and 20 eV, respectively and quantified using empirically derived relative sensitivity factors provided by Kratos analytical. Samples were mounted in floating mode in order to avoid differential charging. Charge neutralization was required for all samples. Binding energies were referenced to the C 1s peak of (C-C, C-H) bond which was set at 284.8 eV. The data were analyzed with commercially available software, CasaXPS.

Micro-Raman spectroscopy exciting the scattering at 633 nm, and collecting the Stokes and anti-Stokes sides, was performed by a Witec Alpha Raman spectrometer (600gr/mm, laser power < 200 μW, OBJ NA=0.9 mag=100X, volume Bragg grating notch filters package) spanning the frequency range from ca. -700 to ca. +2300 cm^{-1}. Several areas of the Mo_2CT_x film surface were imaged obtaining Raman mapping (100x180 μm^2, 100x100 points, 2 sec/pt.).

The resonant Raman scattering spectrum of the bulk Mo_2CT_x multilayered structure was obtained averaging >1000 spectra from inside the inter-electrodes channel, (blue box in **Figure S13d**). While SERS spectra resulting from a single point sampling on the electrodes area constitute and characterize the heterogeneity of the topmost flakes surface. Low-frequency bare Mo_2CT_x spectrum was analyzed, after subtraction of a broad baseline by Lorentzian functions minimization routine retrieving position area and width of the sharp peaks.

The spectral sensitivity measurements were performed by a homemade confocal setup, see **Figure S15a**. A supercontinuum white light laser (superK Extreme, NKT Photonics) was used for the continuous scanning of the 400-800 nm spectral range. Excitation was

monochromatized by an acousto-optic resonator filter (NKT SuperK Select multi-line tunable filter AOTF) allowing for a 4-8 nm bandwidth delivered by a broadband fiber and focused by a 10x Nikon objective. The spot size, thought wavelength dependent, resulted in any condition smaller than 25 μm. Laser intensity was selected in the 1-2 mWatt range, and each current measure was normalized to the actual monitored laser power concurrently recorded by a calibrated power meter as a function of the wavelength. Sample alignment was allowed by a micro stage confocally monitored by a CCD camera. For each spectral point, three measurements were repeated for statistical meaning. At each wavelength the IV characterization was performed applying a sawtooth signal (4 ramps, 1 s/ramp) to the device by a Keithley 2612B SourceMeter® spanning the -1, +1 V bias range, recording the current each 0.1V. Data analysis was performed with the Matlab® software to get the spectral current/mW vs. applied bias. The measure was repeated into three different positions on the sample. For the specific wavelength of 633 nm, we have also performed micro-photocurrent imaging as reported in **Figure S16d** recording the photocurrent at 0.5V bias while scanning the sample below the excitation laser.

The Keithley KE4200-SCS semiconductor characterization system was used to measure electrical and photoresponse characteristics of the devices under ambient conditions. Continuous-wave semiconductor diode laser sources (CivilLaser) were used to generate light at 660 nm and 532 nm wavelengths. A laser power meter (Thorlabs) was used to measure the incident power of the laser pulses. The dark current of the photodetectors were re-measured in vacuum at room temperature, using a Lakeshore vacuum probe station under a pressure less than 1×10^{-5} Torr.

Femtosecond transient absorption setup is detailed elsewhere.[5] Briefly, the white-light continuum probe pulses were generated in a 200 μm CaF_2 nonlinear crystal using intense 800 nm fs laser, and spectrally tunable pump femtosecond pulses (330 nm; a few μJ pulse energy) were generated in an optical parametric amplifier (Light Conversion). The pump and probe

pulses were spatially overlapped on the sample, and the transmitted probe pulse from the samples was collected on the broad-band UV-visible-NIR detectors.

Both atomic-resolution scanning transmission electron microscopy (STEM) imaging and electron energy loss spectroscopy (EELS) investigations were carried out at 80 kV with a ThermoFisher USA (former FEI Co) Titan Themis Z (40-300kV) TEM equipped with a double Cs (spherical aberration) corrector, a high brightness electron gun (x-FEG), an electron beam monochromator, and a Gatan Quantum 966 imaging filter (GIF). Low-loss EEL spectroscopy was performed in a combination with STEM imaging (so-called STEM spectrum imaging or SI) of Mo_2CT_x and $Ti_3C_2T_x$ flakes, drop-casted on silicon TEM grids (SiMPore Inc.) with 5 nm thick Si_3N_4 windows. The low-loss spectra were acquired in so-called microprobe STEM mode with about 1 mrad semi convergence angle. For low-loss EELS the monochromator operation was optimized by the method first implemented in, **ref. 6** and described in details in, **ref. 7**. As a result, mapping of spatial distribution of the SP modes was obtained with the energy resolution of about 45-50 meV (defined as the full width at half maximum of the ZLP), allowing to distinguish spectral features (SPs resonant maxima) in the MIR range directly (without deconvolution of the data). The background subtraction was performed by fitting of ZLP measured on pristine Si_3N_4 (without MXene flakes). Thickness of the studied flakes was derived using the log-ratio method.[8] Following this method, the absolute thicknesses (t) was calculated by knowing the effective inelastic mean free path as described in details in, **ref. 9**.

Spectroscopic ellipsometry measurements were made using J.A. Woollam M2000 (DI) in the range from 193 to 1690 nm, using multiple incident angles 65, 70, and 75. Data were collected on Mo_2CT_x films sprayed on Si substrate with a ca. 100 nm thermal oxide layer (*i.e.* SiO_2). The thickness of the thermal oxide was accurately determined using ellipsometry measurement on the bare substrate, which was subsequently used in the modeling of the Mo_2CT_x film on SiO_2/Si substrate. Data fitting was performed to acquire the optical constants using CompleteEASE software from J.A. Woollam. The Mo_2CT_x layer was fitted with a Drude

component and a set of harmonic oscillators to acquire the real and imaginary components of the dielectric function. The real and imaginary components of the dielectric function of Mo_2CT_x are depicted in **Figure S29**. The fitting parameters are shown in **Table S3**.

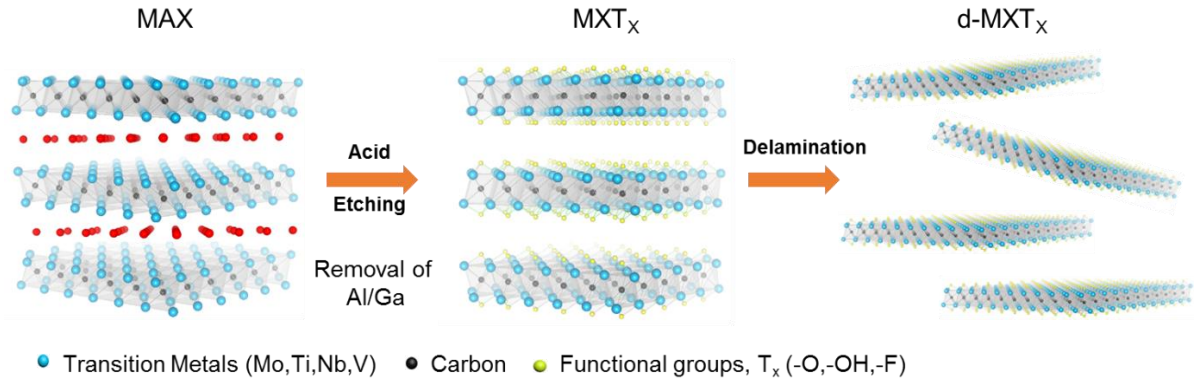

Figure S1. Schematic illustration of the MXene synthesis process.

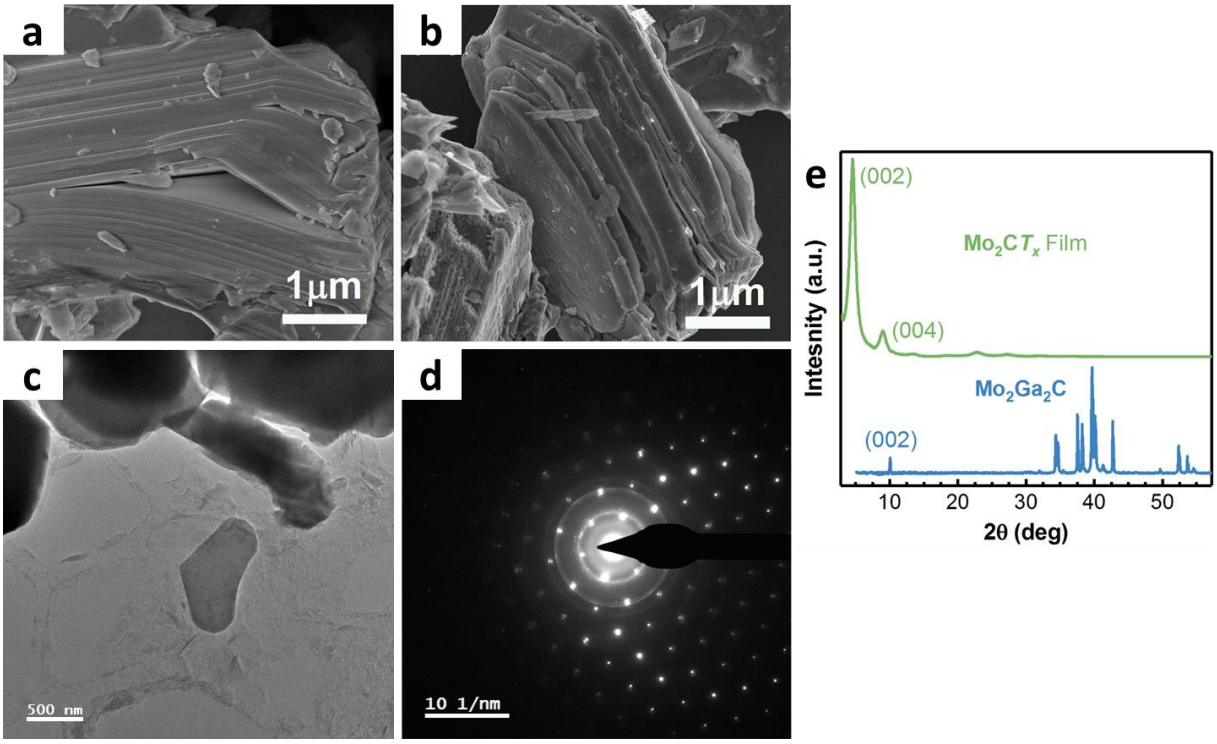

Figure S2. Secondary electron SEM images for **a,** unreacted multilayered Mo_2Ga_2C MAX and **b,** exfoliated Mo_2CT_x. **c,** Bright-field TEM image of a representative Mo_2CT_x nanoheet, and **d,** its corresponding SAED pattern. **e,** XRD patterns of Mo_2Ga_2C MAX (blue) and the corresponding intercalated-Mo_2CT_x MXene film (green).

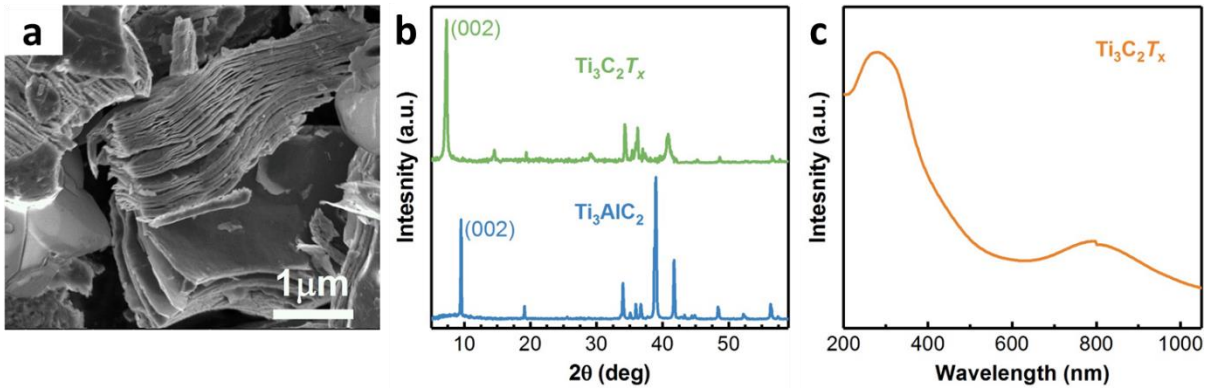

Figure S3. a, Secondary electron SEM image for exfoliated multilayered $Ti_3C_2T_x$. **b,** XRD patterns of Ti_3AlC_2 MAX (blue) and the corresponding $Ti_3C_2T_x$ MXene film (green). **c,** UV-Vis-NIR absorption spectrum of $Ti_3C_2T_x$ nanosheets suspended in water.

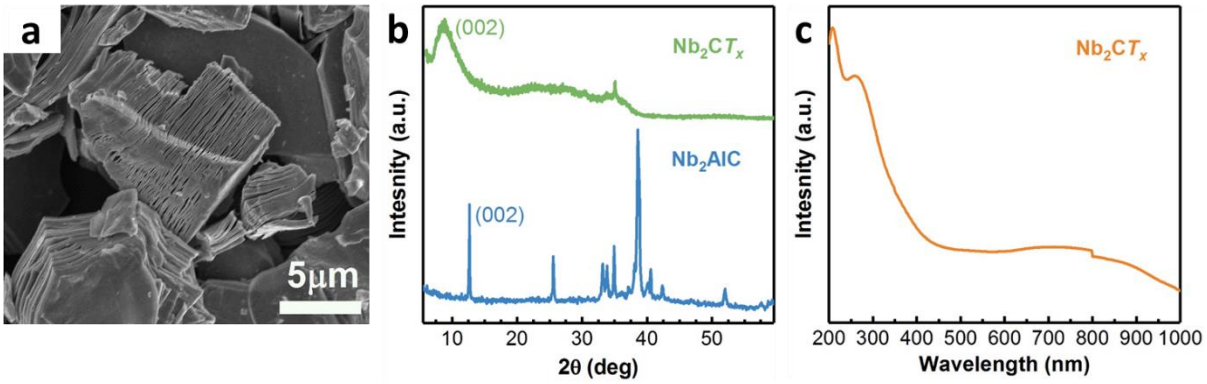

Figure S4. a, Secondary electron SEM image for exfoliated multilayered Nb_2CT_x. **b,** XRD patterns of Nb_2AlC_2 MAX (blue) and the corresponding Nb_2CT_x MXene film (green). **c,** UV-Vis absorption spectrum of Nb_2CT_x nanosheets suspended in water.

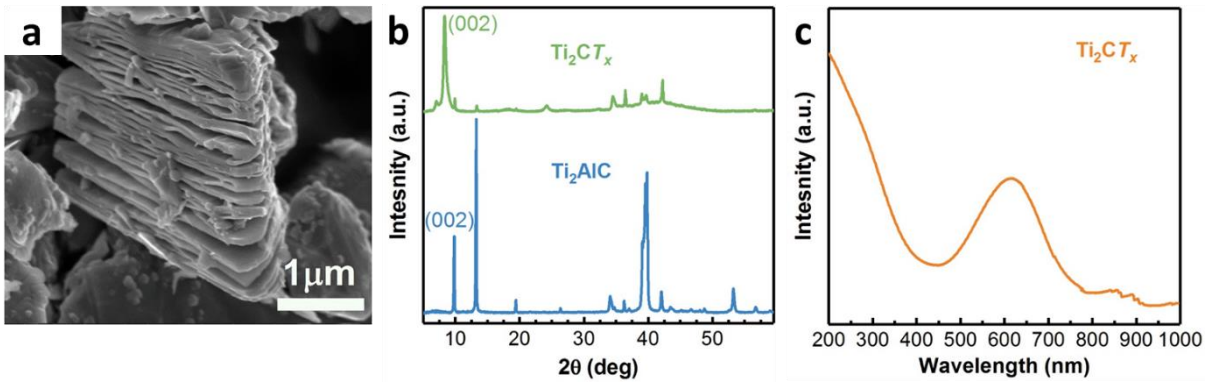

Figure S5. a, Secondary electron SEM image for exfoliated multilayered Ti_2CT_x. **b,** XRD patterns of Ti_2AlC_2 MAX (blue) and the corresponding Ti_2CT_x MXene film (green). **c,** UV-Vis absorption spectrum of Ti_2CT_x nanosheets suspended in water.

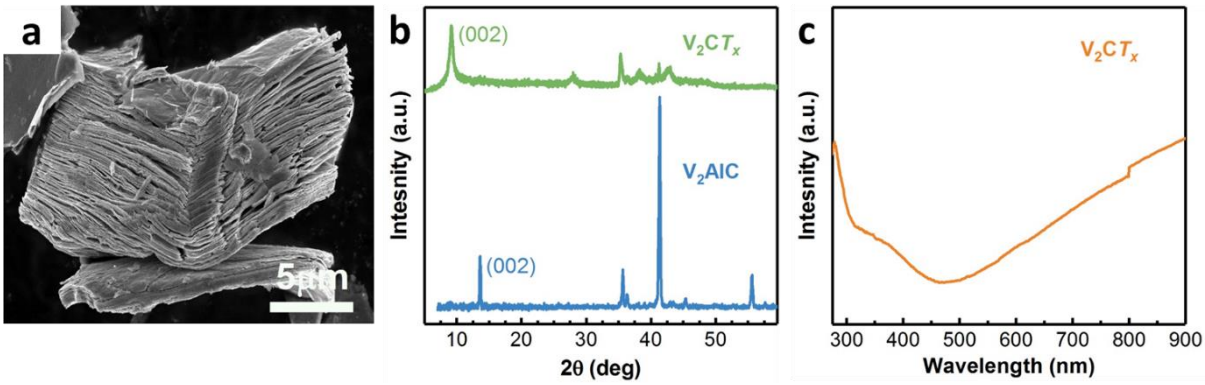

Figure S6. a, Secondary electron SEM image for exfoliated multilayered V_2CT_x. **b,** XRD patterns of V_2AlC_2 MAX (blue) and the corresponding V_2CT_x MXene film (green). **c,** UV-Vis absorption spectrum of V_2CT_x nanosheets suspended in water.

X-ray Photoemission Spectroscopy (XPS)

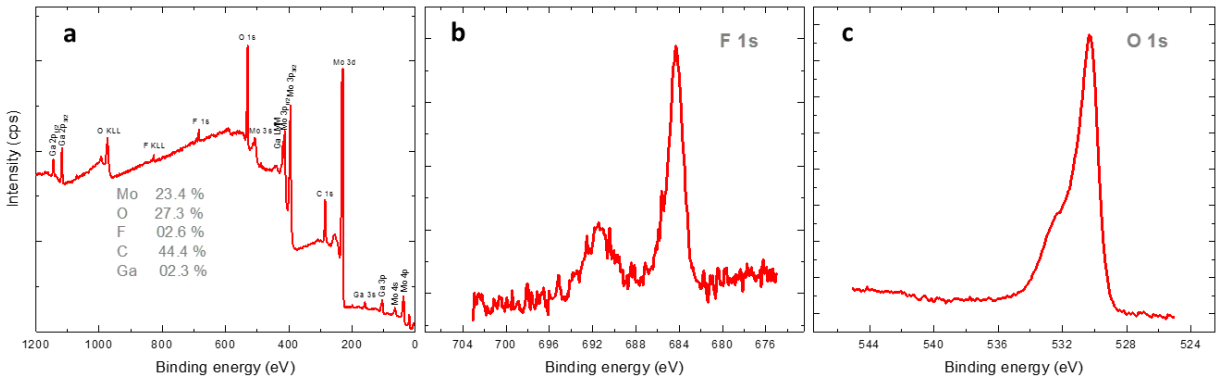

Figure S7. a, Scan survey spectrum of Mo_2CT_x. **b,** High-resolution XPS spectrum of the F 1s core level. **c,** High-resolution XPS spectrum of the O 1s core level.

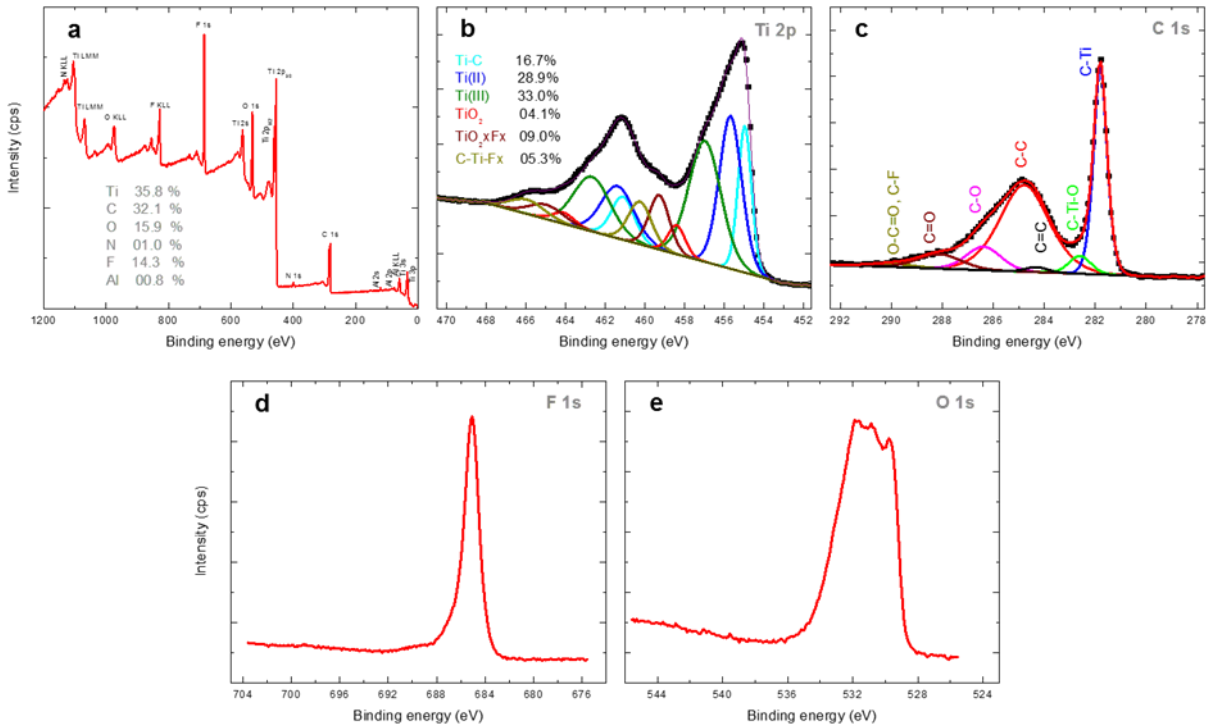

Figure S8. a, Scan survey spectrum of $Ti_3C_2T_x$. High-resolution XPS spectrum of **b,** Ti 2p, **c,** C 1s, **d,** F 1s, **e,** O 1s core levels.

The Ti 2p core level from $Ti_3C_2T_x$ was fitted with six doublets (Ti $2p_{3/2}$ – Ti $2p_{1/2}$) with a fixed area ratio equal to 2:1 and doublet separation of 5.7 eV (except for Ti_C the doublet separation is equal to 6.2 eV). The Ti $2p_{3/2}$ components were located at 455.0 eV, 455.7 eV, 457.0 eV, 458.4 eV, 459.3 eV, and 460.3 eV, respectively. The Ti $2p_{3/2}$ component centered at 455.0 eV is associated with Ti bound to C.[10,11] While the Ti $2p_{3/2}$ components centered at 455.7 eV and 457.0 eV are associated to Ti ions with valence state 2+ and 3+, respectively[10,12]. The Ti $2p_{3/2}$ component centered at 458.4 eV is associated with TiO_2.[12,13] The Ti $2p_{3/2}$ components centered at 459.3 eV and 460.3 eV are associated to Ti from $TiO_{2-x}F_x$ species and to C-Ti-F_x bond, respectively.[12]

The C 1s core level of $Ti_3C_2T_x$ was fitted using seven components located at 281.8 eV, 282.6 eV, 284.3 eV, 284.8 eV, 286.4 eV, 288.1 eV and 290.0 eV corresponding to C-Ti, C-Ti-O, C=C (sp2), C-C/C-H (sp3), C-O, C=O,] and (O-C=O and C-F) bonds, respectively.[14]

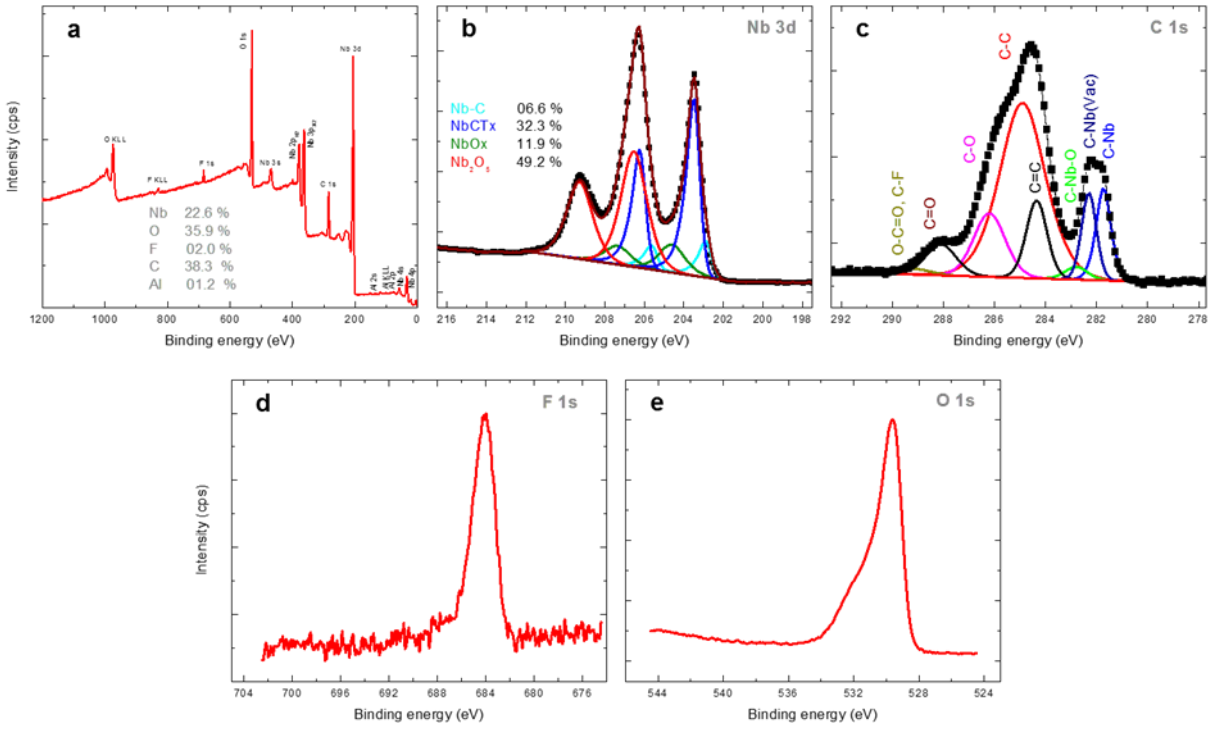

Figure S9. a, Scan survey spectrum of Nb_2CT_x. High-resolution XPS spectrum of **b,** Nb 3d, **c,** C 1s, **d,** F 1s, **e,** O 1s core levels.

The Nb 3d core level from Nb_2CT_x sample was fitted with four doublets (Nb $3d_{5/2}$ –Nb $3d_{3/2}$) with a fixed area ratio equal to 3:2 and doublet separation of 2.75 eV. The Nb $3d_{5/2}$ components were located at 202.9 eV, 203.5 eV, 204.6 eV, and 206.5 eV, respectively. The Nb $3d_{5/2}$ component centered at 202.9 eV is associated with Nb bound to C in Nb_2CT_x,[12,15,16] while the Nb $3d_{5/2}$ component centered at 203.5 eV is associated with Nb bound to C in Nb_2CT_x phase where Nb is bound with surface termination species such as O, OH and/or F.[12,16] The Nb $3d_{5/2}$ components centered at 204.6 eV, and 206.5 eV are associated to Nb in sub-oxides species and to Nb from Nb_2O_5, respectively.[12,16]

The C 1s core level from Nb_2CT_x was fitted using eight components located at 281.7 eV, 282.3 eV, 282.8 eV, 284.4 eV, 284.8 eV, 286.2 eV, 288.1 eV and 289.1 eV corresponding to C-Nb, C-Nb(V_{ac}) (C near a vacancy, or defect), C=C (sp_2), C-C/C-H (sp_3), C-O, C=O and (O-C=O and C-F) bonds, respectively.[12]

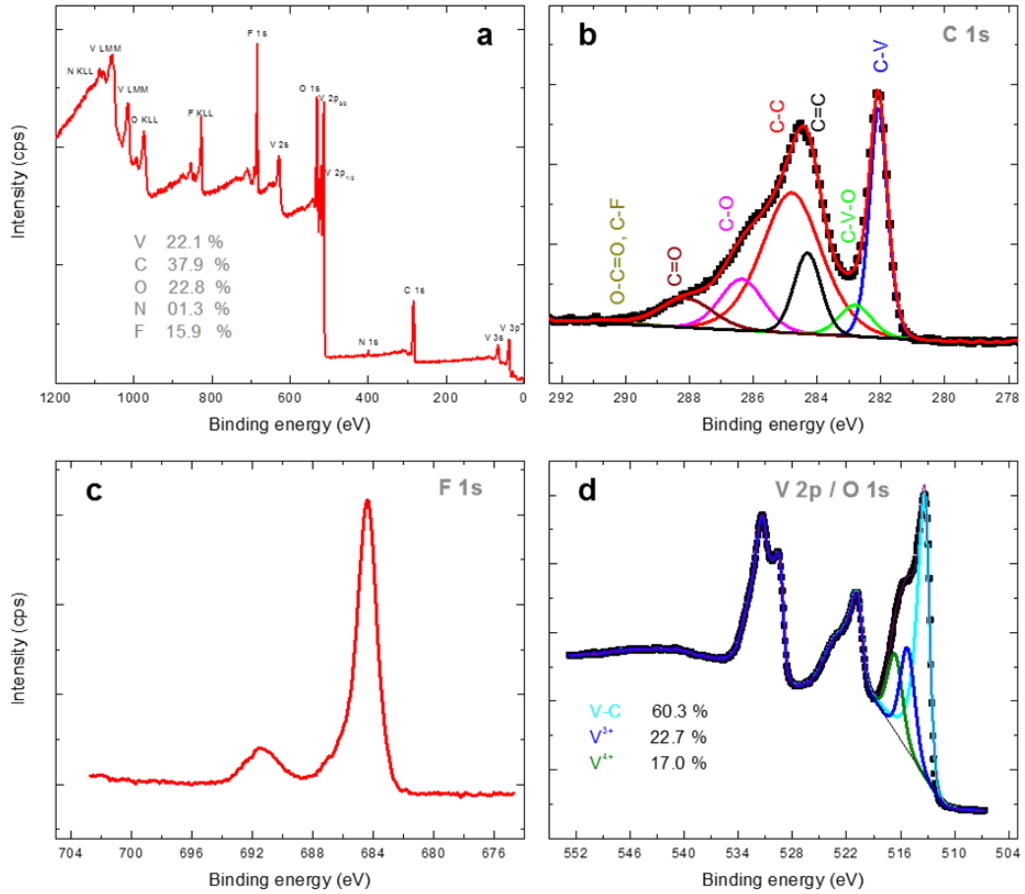

Figure S10. a, Scan survey spectrum of V_2CT_x. High-resolution XPS spectrum of **b,** V 2p / O 1s, **c,** C 1s, **d,** F 1s.

High resolution XPS spectra of V 2p / O 1s and C 1s core levels from V_2CT_x have been obtained. The V $2p_{3/2}$ core level was fitted with three components located at 513.3 eV, 515.2 eV, and 516.2 eV. The V $2p_{3/2}$ component centered at 513.3 eV is associated with V bound to C in V_2C while the components 515.2 eV, and 516.2 are associated to oxidized vanadium with III and IV oxidation states.[13,16,17]

The C 1s core level from V_2CT_x sample was fitted using seven components located at 282.1 eV, 282.8 eV, 284.3 eV, 284.8 eV, 286.3 eV, 288.1 eV and 290.6 eV corresponding to C-V, C-V(V_{ac}) (C near a vacancy, or defect), C=C (sp_2), C-C/C-H (sp3), C-O, C=O and (O-C=O and C-F) bonds, respectively.[12]

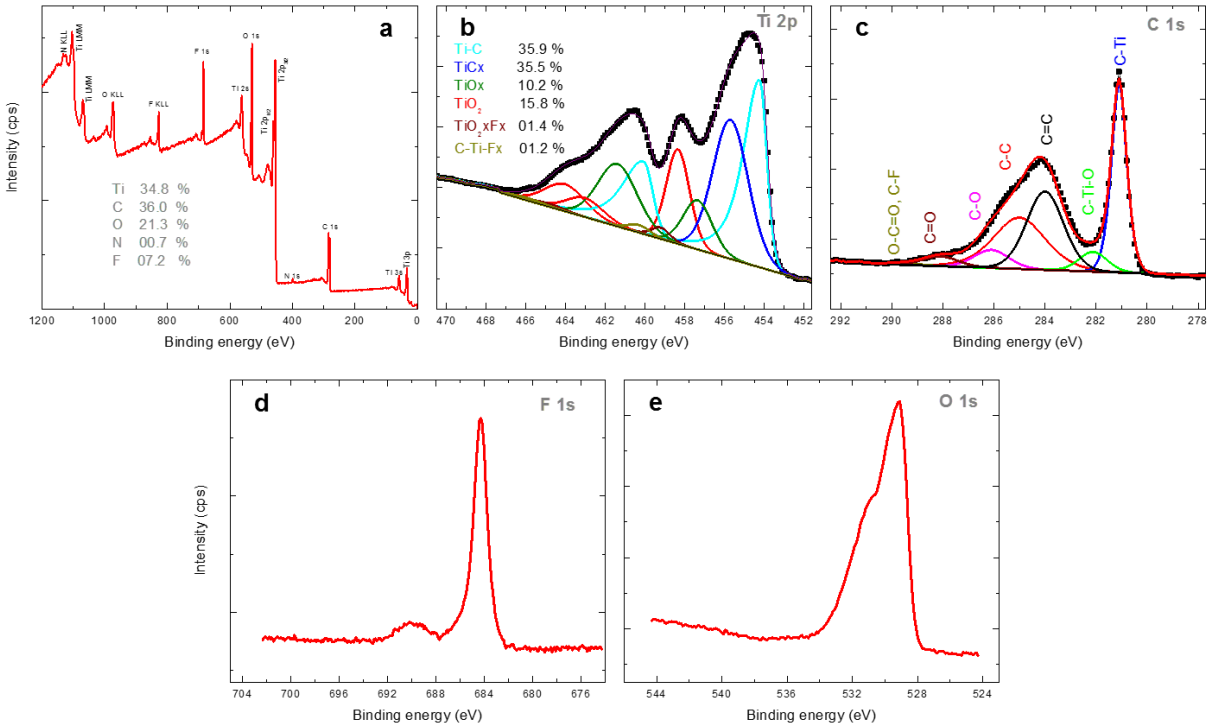

Figure S11. a, Scan survey spectrum of Ti_2CT_x. High-resolution XPS spectrum of **b,** Ti 2p, **c,** C 1s, **d,** F 1s, **e,** O 1s core levels.

High resolution XPS spectra of Ti 2p and C 1s core levels from Ti_2CTx have been obtained. The Ti 2p core level from Ti_2CT_x sample was fitted with six doublets (Ti 2p $2p_{3/2}$ – Ti $2p_{1/2}$) with a fixed area ratio equal to 2:1 and doublet separation of 5.7 eV (except for Ti_C the doublet separation is equal to 5.9 eV). The Ti $2p_{3/2}$ components were located at 454.2 eV, 455.7 eV, 457.3 eV, 458.4 eV, 459.2 eV, and 460.3 eV respectively. The Ti $2p_{3/2}$ component centered at 454.4 eV corresponds to Ti-C bond in T_2CT_x.[18-20] While the Ti $2p_{3/2}$ component centered at 455.7 eV can be assigned to Ti-C_x peak (a combination of a sub-stoichiometric TiC_x (x<1) and to titanium oxycarbides TiC_xO_y.[21] The Ti $2p_{3/2}$ components centered at 459.2 eV and 460.3 eV are associated to Ti from $TiO_{2-x}F_x$ species and to C-Ti-F_x bond, respectively.[11]

The C 1s core level was fitted using six components located at 281.1 eV, 282.1 eV, 284.2, 284.9 eV, 286.2, 288.1 and 289.6 corresponding to C-Ti[19,22], C-Ti-O, C=C (sp2), C-C/C-H (sp3), C-O, C=O and (O-C=O and C-F) bonds, respectively.[14]

Raman Scattering Investigation

We characterized the Mo_2CT_x samples using micro-Raman spectroscopy in the range of -700 to +2300 cm^{-1}, exciting the inelastic scattering at 633 nm, and collecting the Stokes and anti-Stokes sides. The analysis allowed the identification of distinctive bulk-polycrystalline and surface-bonded molecular vibrations, as well as their spatial distribution and homogeneity by hyperspectral imaging analysis. Various gold-MXene junctions as well as different MXene areas were imaged within a window of 100x180 μm^2 (100x100 points) at scanning rate of 2 sec/pt. **Figures S12b** and **c** show the reconstructed assignment with relevant intensity maps of the two spectra shown in **Figure S12a**, which are obtained from cluster analysis. Based on this analysis, we directly obtained an accurate spectrum for the bare MXene film (nanosheets-bulk) dominated by the $2E_{1g}$ and A_{1g} symmetry vibrational modes of Mo_2CT_x with a minor presence of the parent MAX precursor. We have also collected various surface enhanced Raman scattering (SERS) spectra, obtained at different positions on the gold electrodes (obtained by sputtering of a nominal 50 nm Au-layer on Mo_2CT_x). The spatially-averaged SERS spectrum (red one in **Figure S12a**) shows a rather small presence of the bulk fingerprint superimposed with a broad unstructured band with the expected D, G and D' bands, which are typical for carbon materials, at about 1350, 1580 and 1620 cm^{-1}, respectively.[23]

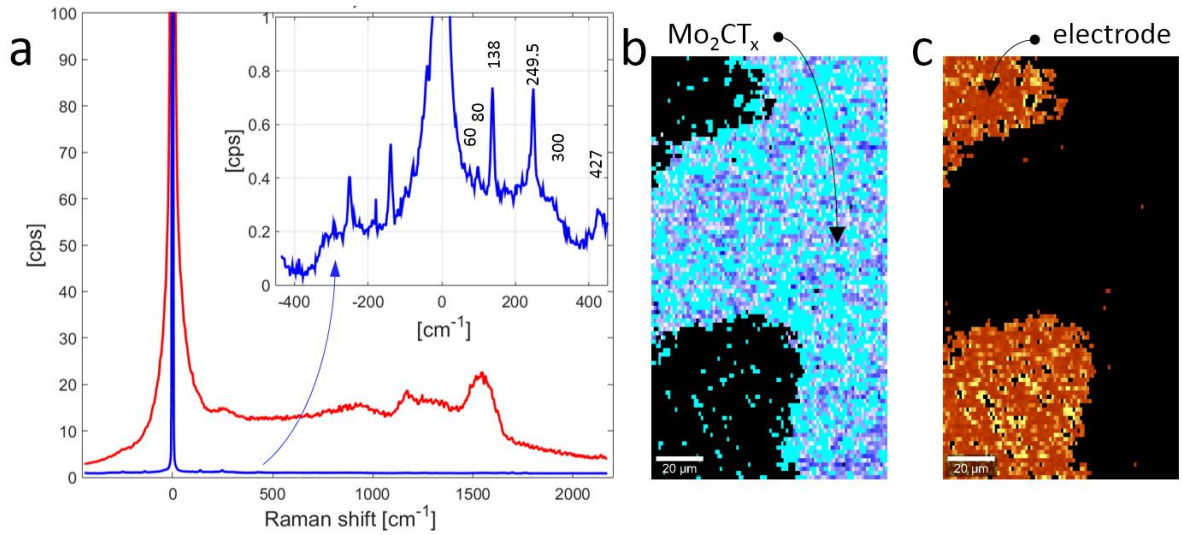

Figure S12. Micro-Raman imaging (a 100x100 pts window) of a Mo_2CT_x Mxene photodetector with an area of 100 x 180 mm^2. **a,** The two significant components, determined by cluster analysis, obtained at the bare Mo_2CT_x film (bulk, blue spectrum) and at the electrodes (spatially-averaged SERS, red spectrum). Note the differences between the shape and the intensity profile of the two spectra as a result of the SERS-effect induced by the Au-electrodes. Inset: low-frequency fingerprint of Mo_2C network. **b,** Normalized intensity map (black 0%, light blue 100%) of polycrystalline Mo_2CT_x nanosheets (bulk). **c,** Normalized intensity map (black 0%, orange 100%) of the SERS spectrum as from cluster analysis. Orange areas indicate intense SERS scattering signals and offer a visual distribution of active hot spots.

The low-frequency Raman scattering from bare Mo_2CT_x (inset of **Figure S12a**), though of very small intensity, accesses the molecular vibrational modes of the Mo_2C network. It is also populated with shear and interlayer breathing modes that contribute to the unstructured and intense quasi-elastic scattering signals recorded below ca. 60 cm^{-1}. To note, the Brag diffraction gratings we used to access the low-frequency Raman spectrum allow an elastic-free Raman spectrum down to 8 cm^{-1}.

The presence of the sharp peaks, demonstrated in **Figure S13**, confirms the polycrystalline structure of Mo_2CT_x and allows to define its (bulk) fingerprint (obtained by averaging more than 1000 spectra collected from an extended area; blue frame in **Figure S13d**). The whole spectrum (blue one in **Figure S13a**) is composed of a fluorescence baseline superimposed with the crystal fingerprint and a quasi-elastic peak, which is typically observed

in glasses and in disordered systems. This strong quasi-elastic peak is certainly indicative of the residual defects-rich structure constituting the samples.

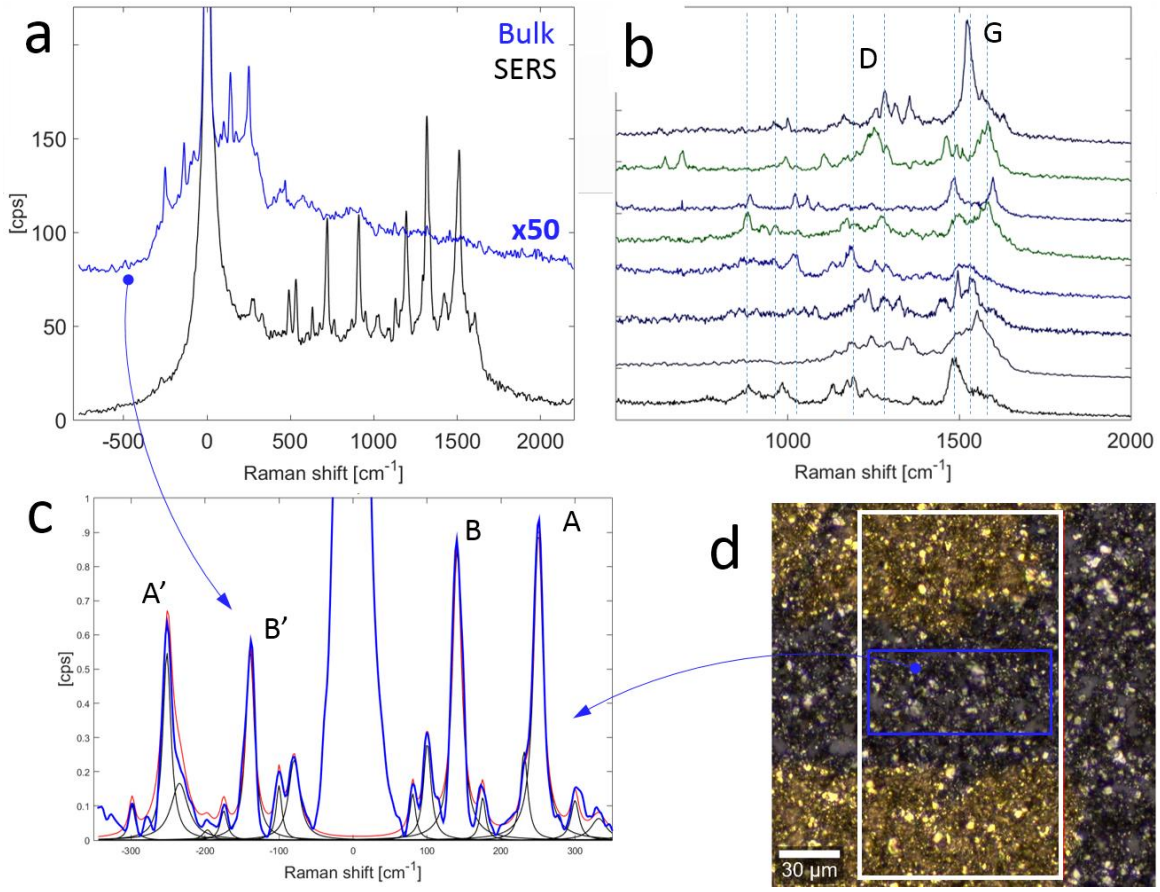

Figure S13. Micro-Raman spectroscopy characterization of Mo_2CT_x at 633 nm. **a,** (Blue) resonant Raman scattering spectrum of (Bulk) Mo_2CT_x multilayered structure (50x) obtained by averaging more than 1000 spectra. The excited area of the Mo_2CT_x film lie between the inter-electrodes channel (within the blue frame shown in **Figure S13d**). (Black) One SERS spectrum displayed for comparison. **b,** Heterogeneous collection of SERS spectra obtained at different positions on the Au-electrodes (within the white frame shown in **Figure S13d**). **c,** Low-frequency range of the Raman spectrum of the bare Mo_2CT_x film. The spectrum is analyzed by Lorentzian functions after subtraction of the broad baseline. The unexpected S/AS ratios for AA' and BB' vibrations evidence an active photon-electron-phonon anisotropic resonance process that occurs in Mo_2CT_x. **d,** An optical image of the sample. The white frame indicates the total mapped area, while the blue frame encircles the area considered for the Mo_2CT_x Raman fingerprint determination.

In accordance with the previous studies,[24,25] we have been able to gain a better insight about the structural arrangement of our Mo_2CT_x by identifying most of the Raman shifts (bulk and SERS, sampled from different areas), related to Mo carbides and oxides. We did not only look for strong, intense peaks of Mo_2CT_x, but also of Mo_2GaC and Mo_2C as well as Mo-oxides (e.g. MoO_2 and MoO_3). In **Table S1**, we show the Raman shifts of ten vibrations, measured with high accuracy, along with their symmetry assignment. The two most intense low-frequency peaks, at about 140 (B) and 250 (A) cm^{-1}, are attributed to the in-plane ($2E_g$) and to the out-of-plane (A_{1g}) vibrational modes of the Mo_2C layer, respectively, that are dominated by the motion of heavy Mo atoms. A schematic representation of the A_{1g} and $2E_g$ vibrational modes, is displayed in **Figure S14h**. The minor peaks, yet visible, at 175 and 233 cm^{-1} (shown in **Figure S13c**) are ascribed to the vibrational modes of traces of the Mo_2Ga_2C phase.

It is clear that the characteristic modes of the Mo_2C network strongly couple with those of the functionalized surface structures, Mo_2CT_x (T_x: F, O, and OH), that mainly characterizes the surface chemistry of our Mo_2CT_x film as reflected by the point-to-point variation in its corresponding SERS spectra (**Figure S13b**). There are many possible structural combinations and thus, possibly, crowded vibrational Raman spectra are expected that reflect different masses and bond strengths of the T_x atoms. This complex surface structural variations have led to the obvious heterogeneous nature of the Mo_2CT_x surface as demonstrated in **Figure S13b**.

The DFT models that are introduced in the literature to evaluate the stability of the Mo_2CT_x's electronic structure (obtained by varying the lattice positions of the functional groups (T_x)),[26] have predicted distinct acoustic dispersions and Raman active modes for Mo_2CT_x. The corresponding reported frequency shifts (e.g. $2E_g$ modes of Mo_2CO_2 at 63 cm^{-1}, and of Mo_2CF_2 at 77 cm^{-1}) are on par with the peaks we identified at ca. 60, 80, 100, 300 and 330 cm^{-1}, confirming the presence of such modes in our spectrum. Moreover, contributions from O-terminated surface vibrations (Mo_2CO_2), in particular, are also expected at the intermediate- and high-frequency regimes as indicated by the strong bonds of Mo-O and Mo=O at ca. 430

and 920 cm^{-1}, respectively (see **Figure S12a**). Our experimental results have also shown the presence of other chemical bonds such as C-F at ca. 720-800 cm^{-1}, and MoO_3 at ca. 830 cm^{-1}, which correlates well with the XPS results (**Figures 1i** and **1j**). The relatively strong intensity of the peak at 830 cm^{-1} is attributed to the expected resonance Raman enhancement for MoO_3 nanoparticles due to their known resonant coupling to the electronic absorption at ca. 2 eV (~633 nm). On the other hand, we do not see significant traces of bare Mo_2C nanoparticles, which are generally characterized by three intense peaks at 695, 828 and 1006 cm^{-1}.

Table S1. Low-frequency Raman shifts of Mo_2CT_x obtained by Lorentzian shape analysis of the experimental Raman spectrum shown in **Figure S13** and described in the above text.

Peak	1	2	3	**4 (BB')**	5	6	**7 (AA')**	8	9	10
Shift [cm^{-1}]	60±2	80.1±1.2	100.2±0.7	139.7±0.4	175±1.5	233±3	250.5±0.3	299±3	331±3	427
S/AS (area)				1.7 ± 7%			1.3 ± 6%			
Assignment	Mo_2CO_2 $2E_g$	Mo_2CF_2 $2E_g$	Mo_2CT_x $2E_g$	Mo_2C $2E_g$	Mo_2Ga_2C $2E_g$	Mo_2Ga_2C A_{1g}	Mo_2C A_{1g}	Mo_2CT_x	Mo_2CT_x	Mo-O

Furthermore, the sharp peaks in the low-frequency range, distinct from the other broader components in the spectrum, have demonstrated anomalously low Stokes and Anti Stokes (S/AS) intensity ratios; ca. 1.3. This value is rather far from what can be estimated (ca. 10) for considered peaks couple, in the lowest order Raman process approximation ($\Delta\nu_{S\text{-}AS}$ =500 cm^{-1}), following the Bose-Einstein statistics applied to bosonic thermal phonons. Such low S/AS intensity ratios underline an interesting phenomenon occurring in the MXene. In principle, the Bose-Einstein statistics, in a linear Raman scattering regime, allow for the estimation of the S/AS intensity ratios at finite temperature T, considering the phonon occupation number. In general, in the lowest order Raman process there is photon absorption from the electronic system that generates an electron-hole pair. That pair creates or absorbs a phonon in the atomic system (Stokes or anti-Stokes phonon of energy, $\hbar\omega$) and finally recombines to emit a photon that carries the structural information. In the classical field theory, the electron-photon

interactions introduce a factor proportional to the fourth power of the frequency, so that S/AS intensity ratio expresses as:

$$\frac{I_S}{I_{AS}} = \frac{\omega_S^4}{\omega_{AS}^4} e^{\frac{\hbar\omega}{K_B T}}; \quad K_B T@\ 298K\ \approx 207\ cm^{-1}$$

We propose that such behavior is attributable to the photon-resonance absorption that populates excited molecular electronic states. Such resonance affects the typical anisotropy of 2D layered materials; a fact evidenced by the significantly different S/AS ratios for the indicated peak couples, i.e. AA' and BB', in **Figure S13c**. Noticeably, the vibration corresponding to the AA' pair experiences the effect of such resonance more than the one of BB', which can be expected from vibrations representing out- and in-plane atomic motions. This experimental observation provides some insights into the lattice dynamics and electronic structures of the MXene. In general, the photon-electron-phonon coupling is central to the understanding of fundamental properties of condensed-matter systems, and continues to be an open topic for two-dimensional material research.

Next, we focused on the high-frequency spectral range (>600 cm^{-1}), typical for organic and carbon structures. It is noteworthy that the vibrations in that spectral range is below the sensitivity of this technique, as noticed in the bare Mo2CTx spectrum (**Figure S13a**). However, when the laser is shined on the gold electrodes (50 nm thick layer), the plasmonic material (gold) allows for local SERS revealing the surface chemistry of the underneath Mo_2CT_x.The corresponding signal is particularly intense at the edges of the nanosheets and in between the metalized nanosheet gaps, as shown in **Figure S13d**, and **Figures S14b-d**, where we report the integrated spectral intensity maps of specific energy intervals. The comparison between the obtained spectral images and the optical image of the scanned area (**Figure S14a**), correlates with the observed SERS phenomenon. In SERS imaging, the signal coming from isolated nanometric-sized hot spots characterizes the topmost surface of the device highlighting the chemical variability of the Mo_2CT_x surface. This has been illustrated by the distinct SERS

spectra shown in **Figure S13b**, which are collected at different positions on the electrodes. In the SERS spectra, we have observed a set of strong Raman signals attributed to the carbon matrix and MoO_{3-x} nanocrystals[27,28] as well as the random functionalized surface structures of Mo_2CT_x (T_x: F, O, and OH). However, due to the variable intensity and spatially random nature of the SERS effect from the electrodes, it is not possible for us to properly quantify the content of species at the surface. A further detailed vibrational assignment along with the observed anomalous behavior, will be the argument of a forthcoming investigation.

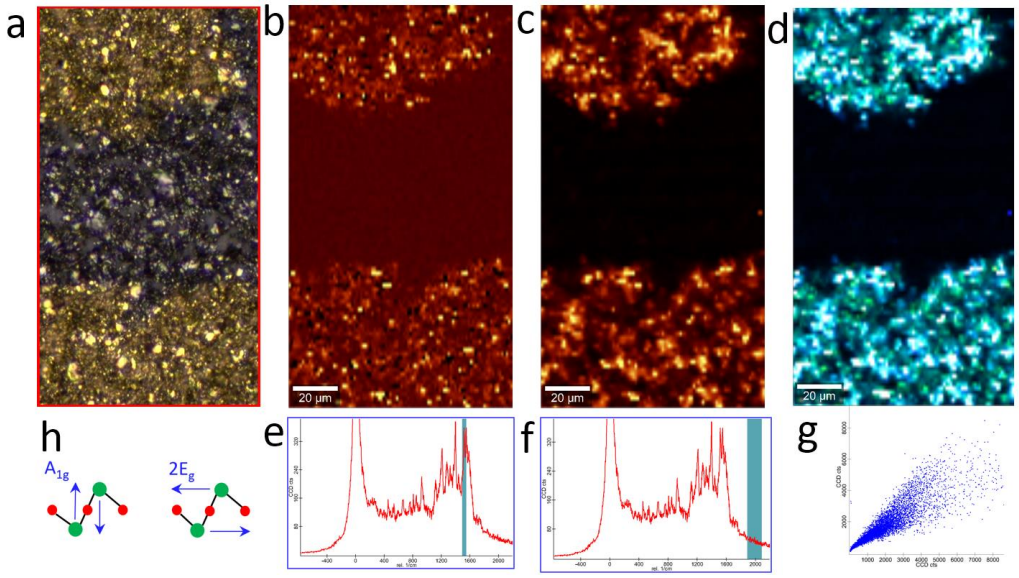

Figure S14. a, Optical image of the Mo_2CT_x sample with a scanned area of 100x1800 μm^2 extending over the electrodes. **b,** Integrated intensity map of the spectral range indicated in e around 1500 cm^{-1}. **c,** Integrated intensity map of the unstructured fluorescence indicated in f. **d,** Combination of the intensity maps in b and c. It shows that only partial correlation can be measured between the SERS signals and fluorescence, as quantified by the correlation intensity comparison reported in **g**. **h,** Schematic representation of the A_{1g} and $2E_g$ vibrational modes.

Photoresponse Characterization

We measured the spectral sensitivity as a function of wavelength on the broadband visible range of MXene thin films as discussed in the main text. Here we focus on the spectral photocurrent and photocurrent imaging under bias obtained for the Mo_2CT_x device.

The experimental setup, shown in **Figure S15a** and **S16a**, allowed to record the current while scanning the 400-800 nm spectral range continuously *via* a supercontinuum white laser excitation focused by a 10x objective. The spot size, though wavelength dependent, is smaller than 25 μm under any condition. The used spot size allowed to obtain the photoresponse from a well representative excitation area of the sample, at a position centered in between the electrodes (apart 70 μm), see **Figures 2a** and **S15b**. A better understanding of the photoresponse was achieved by comparing the result obtained in the previous configuration with those obtained illuminating the electrode partially, or using a large spot size (~300 μm in the case of the yellow spectrum shown **Figure S15b**) by simply defocusing the illumination.

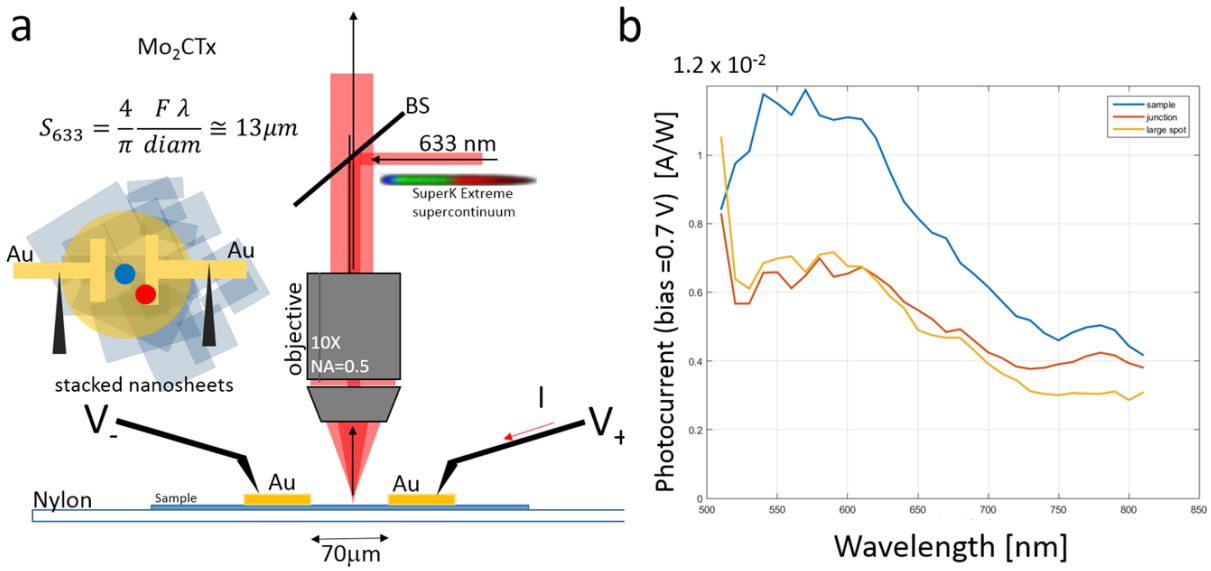

Figure S15. a, Schematic illustration of the experimental photocurrent setup. Inset: Top-view of the device with three different illumination spots: blue (between the electrodes), red (junction, partially on one electrode) and yellow (large spot covering the whole device), considered to determine the spectral photocurrent response of the device reported in b. **b,** Spectral photocurrents profiles at the three different illumination spots shown in **a**.

For the specific wavelength of 633 nm, we have also performed micro-photocurrent imaging, as displayed in **Figure S16**, recording the photocurrent at 0.5V bias while scanning an area larger than the inter-electrodes channel (**Figure S16c**). The current profile (**Figure S16e**), a vertical section from the image shown in **Figure S16d**, shows a rather homogeneous current maximum at the center, in agreement with the spectral data (**Figures 2a** and **S15b**). The current profile is smoothly reduced toward the electrodes, being superimposed to a current ground level, as determined by the DC-dark signal of the same applied bias.

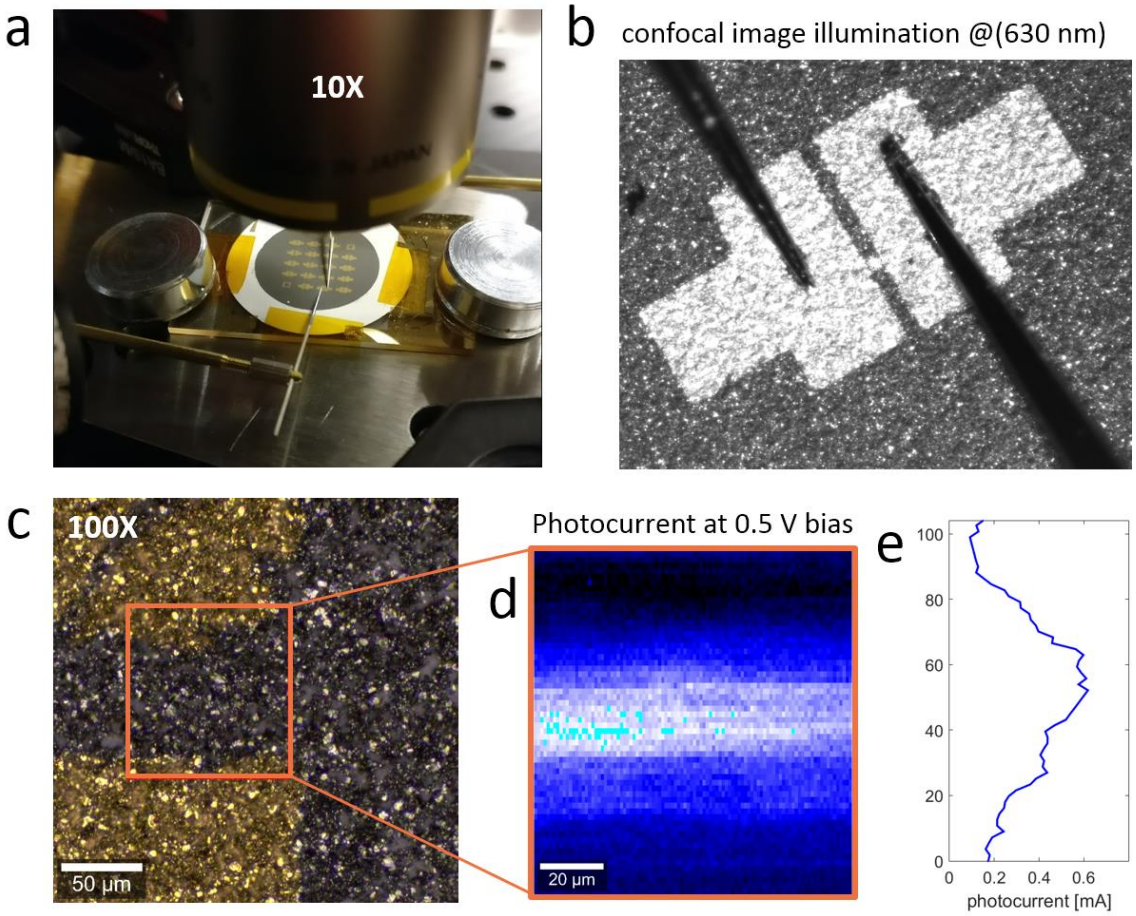

Figure S16. a, Photograph of the photocurrent setup showing one of the investigated samples, illumination objective and the contact electrodes. **b,** Zoomed image of the device under measurement. Note the scattered light from the laser spot shining on the inter-electrodes channel. **c,** Optical image of the sample investigated during the micro-photocurrent imaging. **d,** Photocurrent map, and **e,** vertical current profile.

Table S2. The equations used in the calculation of photodetector properties.

Properties	Equations	Remarks
Responsivity (R): Ratio of the photocurrent generated in the detector to the incident light power.	$R = \Delta I/(P \times A)$	$\Delta I = I_{light} - I_{dark}$ P = *Light intensity* A = *Active area of the device*
Specific Detectivity (D*): The sensitivity of a photodetector.	$D^* = R \times A^{1/2}/(2 \times q \times I_d)^{1/2}$	R = *Responsivity* A = *Active area of the device* q = *Absolute value of electron charge* I_d = *Dark current*
External Quantum Efficiency (EQE): Ratio of the number of photogenerated carriers to the number of photons illuminating the device that produce the photocurrent.	$EQE = \left(\frac{h \times c}{e \times \lambda}\right) * R$	h = *Planck's constant* c = *Velocity of light* e = *Electronic charge* λ = *Incident light wavelength*

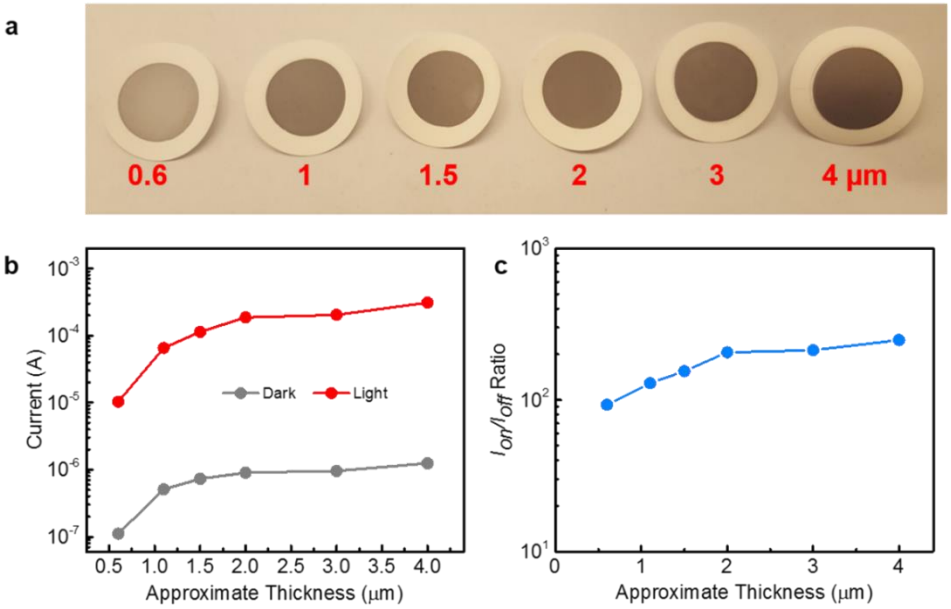

Figure S17. a, Photograph of the Mo_2CT_x thin films with different thickness. **b,** dark current and photocurrent of the Mo_2CT_x thin films as a function of different film thickness. **c,** Ratio of the photocurrent to the dark current of the Mo_2CT_x thin films as a function of different film thickness.

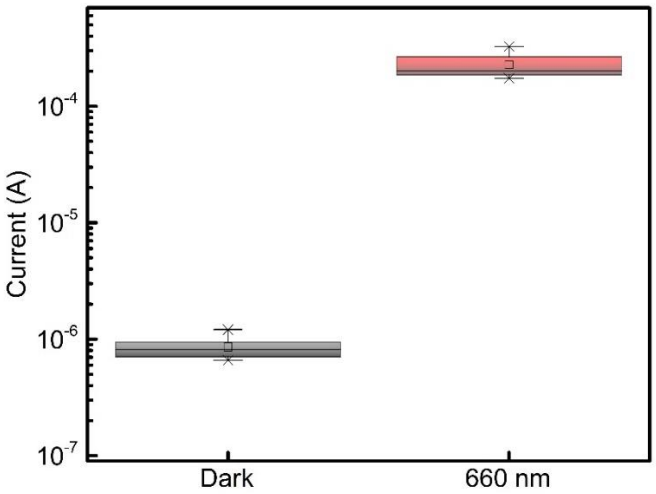

Figure S18. Box-whisker plot of the distribution of the Dark and photocurrent values of the Mo_2CT_x thin films at the wavelength of 600 nm with the light intensity of 0.39 W cm^{-2}. 15 devices examined from 3 different batches showed very slight variations in dark and photocurrent current values.

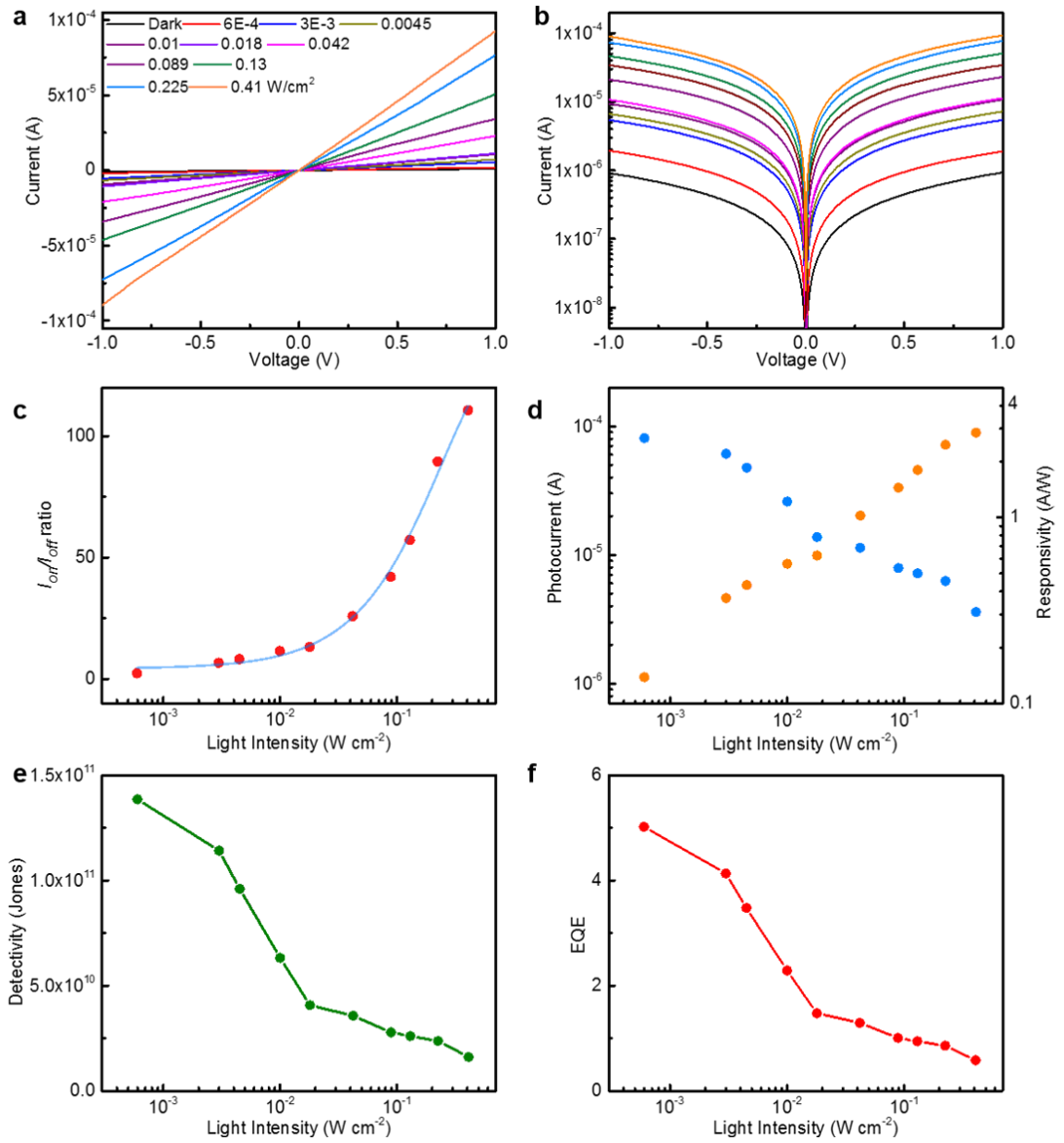

Figure S19. a, Linear **b**, semi log scale current-voltage (*I*–*V*) characteristics of the Mo_2CT_x thin film photodetector in the dark and under different light intensities of visible light at a wavelength of 532 nm with a bias voltage of ±1 V. **c**, ratios of the photocurrent to the dark current of the Mo_2CT_x thin film photodetector as function different light intensities. **d**, (Left) Photocurrents of the Mo_2CT_x thin film photodetector as a function of different light intensities corresponding to the dark state of the device. (Right) Responsivity of the photodetector as a function of different light intensities. **e**, The detectivity and **f**, EQE of the photodetector as a function of different light intensities.

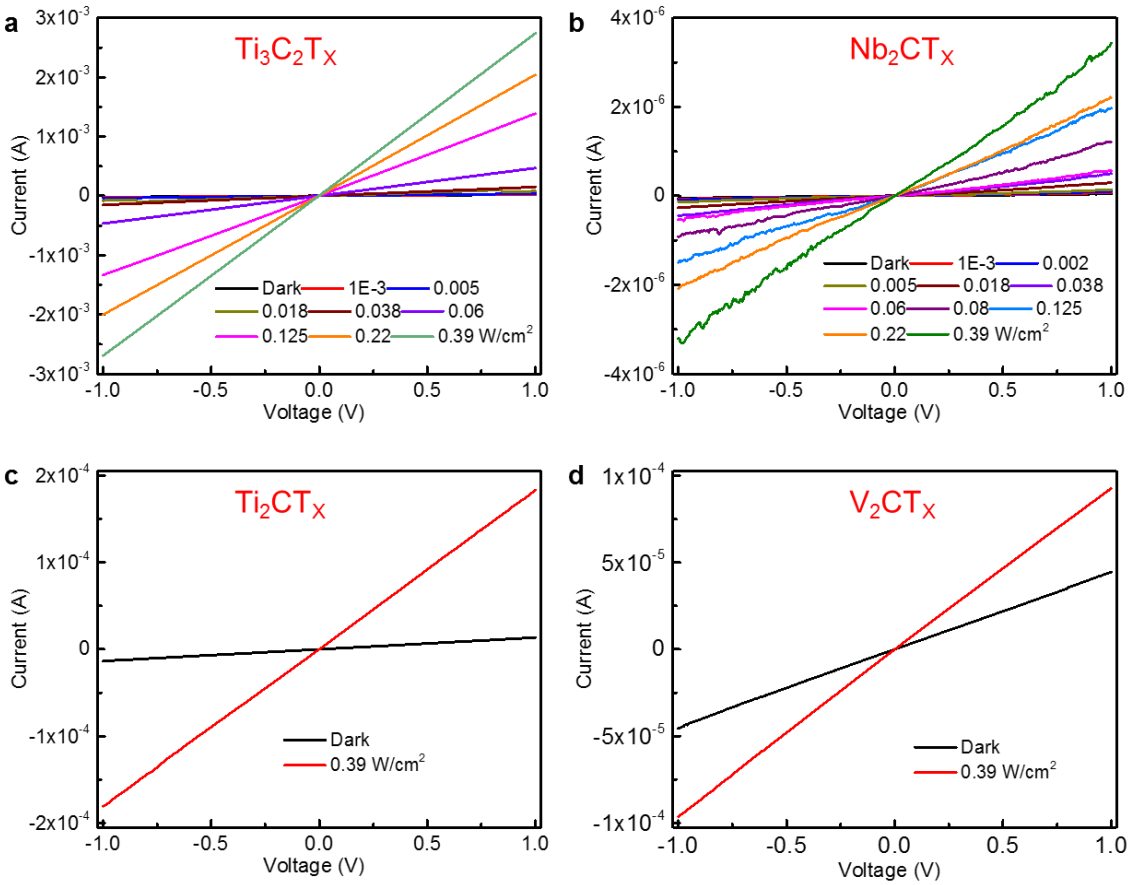

Figure S20. Photodetectors with various MXene thin films. **a**, $Ti_3C_2T_x$ **b**, Nb_2CT_x **c**, Ti_2CT_x **d**, V_2CT_x. Current-voltage (*I*–*V*) characteristics of the MXene thin film photodetectors measured in the dark and under visible light at a wavelength of 660 nm with a bias voltage of ±1 V with 0.39 W cm^{-2} light intensity.

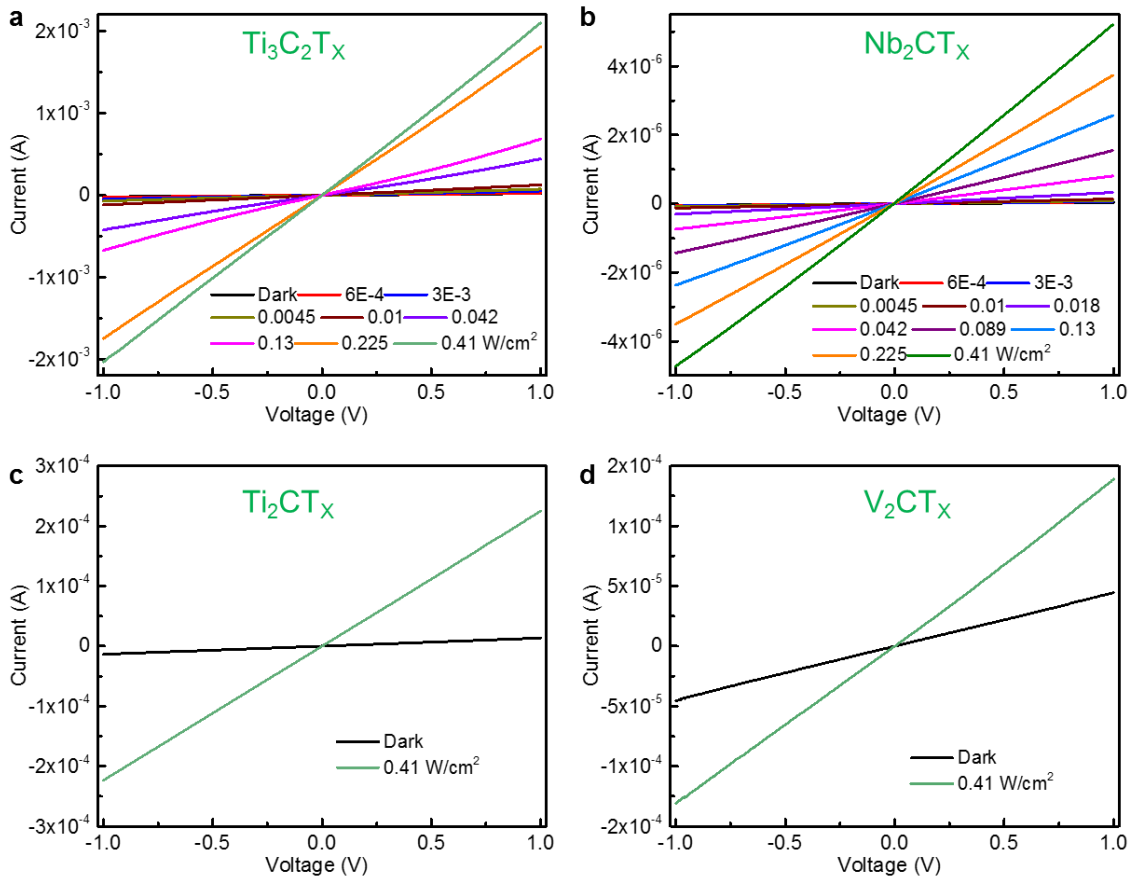

Figure S21. Photodetectors with various MXene thin films. **a**, $Ti_3C_2T_x$ **b**, Nb_2CT_x **c**, Ti_2CT_x **d**, V_2CT_x. Current-voltage (*I*–*V*) characteristics of the MXene thin film photodetectors measured in the dark and under visible light at a wavelength of 532 nm with a bias voltage of ±1 V with 0.41 W cm^{-2} light intensity.

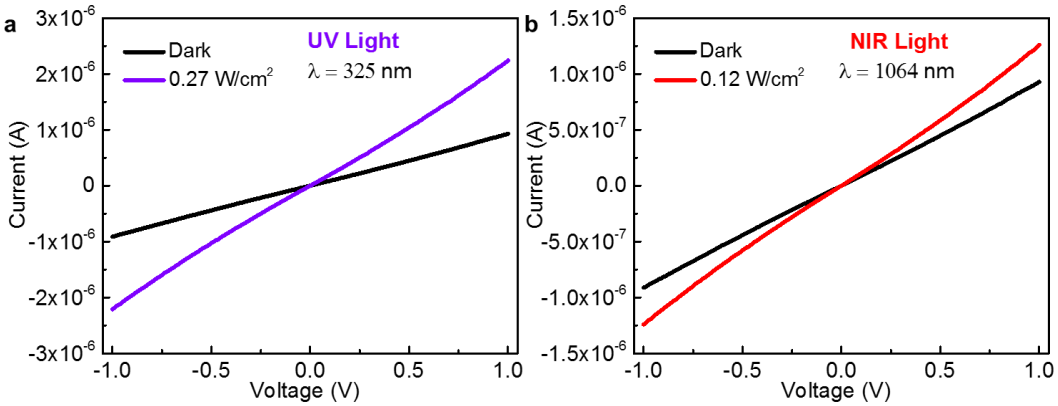

Figure S22. Current-voltage (*I*–*V*) characteristics of the Mo_2CT_x MXene thin film photodetectors measured at wavelengths of 325 nm and 1064 nm of 0.27 W cm^{-2} and 0.12 W cm^{-2} light intensity, respectively.

Physical electromechanical comparison between multilayer Mo_2CT_x nanosheets and gold

To better explain our hypothesis, we compared the physical electromechanical properties of a multilayer Mo_2CT_x cluster, as characterized in **Figures 1b**, **1c**, **3a** and **S2b**, with a typical conventional plasmonic material, i.e. gold. Both are good conductors, with an electron density $> 10^{20}$ and 10^{24}, respectively, meaning that in principle, both can sustain electronic plasmon oscillations. For a few micron scale thickness slab of gold, we can have either bulk or surface plasmon excitations, yet quite different in the physical description. One is a bulk unbounded collective wave of electrons, while the other is a confined excitation at the interface with a dielectric material, characterized by evanescent fields in both media.

On one hand, gold, a typical example of 3D plasmonic material, is known for its properties to locally enhance the electric field by one or more orders of magnitude. When reduced to plasmonic nanostructures, either in a 1D, 2D or 3D nano-confinement, they generate a large amount of hot plasmonic carriers exploiting SPs and their dephasing.[29,30] On the other hand, it is natural to describe the a multilayer Mo_2CT_x cluster as a stratified system of a tightly stacked packet of alternating conductive and dielectric layers, that have inherited their electromechanical properties from their fundamental building unit (i.e. single monolayer). Accordingly, akin in multilayered MoS_2 flakes, it is straightforward to expect a stratification of molecular electronic clouds that essentially have a 2D character each, and a strong anisotropy in the electronic conduction with a reduction of some orders of magnitude in the transversal layer direction. However, owing to their weak interlayer coupling, this anisotropy is expected to be much stronger in MXenes. Previous reports have already demonstrated that, when isolated properly (i.e. fully intercalated), MXene monolayers (specifically $Ti_3C_2T_x$) act as independent polarizable sheets. This phenomenon precisely reveals the true 2D nature of MXenes, underlining the fundamental difference from conventional plasmonic metals.[9,31]

In other words, composed of periodically distributed few atomic-thin structures with a size and interlayer spacing much smaller than the wavelength of interest, and considering the

obtained photoresponse, each stack of multilayer Mo_2CT_x nanosheets can be described with some extent as a natural *plasmonic metamaterial* with a SP character defined by the electrons confinement in the ordered layered planes.

However, due to the difficulty of isolating a single Mo_2CT_x monolayer, its spectral photoabsorption remains to be unknown. Nevertheless, to fit with the scope of this work, we can proceed considering our elemental building unit to be a stack of multilayered-Mo_2CT_x, retrieving its structural and absorption information from TEM imaging as well as the collected experimental photoresponse data. The dimensional statistical analysis of the stacked nanosheets, as obtained from STEM imaging, indicates thicknesses and lateral lengths of values spanning rather broad ranges, 40-150 nm, and 260-2000 nm, respectively. Meaning that the thinnest nanosheet (ca. 40 nm) is actually composed of a large number of stratified monolayers (monolayer thickness is ca. 1 nm). Thus, at least for the investigated Mo_2CT_x photodetectors, we can safely attribute the photoresponse to the collective plasmonic behavior of the stratified multilayered nanosheets rather than that of a mono- or few-layered systems. Moreover, owing to the match between the operational spectral range of our devices and the transversal SP mode (size- and thickness-independent), our attribution is further validated. With this in mind, considering a representative value of ca. 100 nm for the average thickness, we can consider that the 2 μm thick photodetector (in average and all along its extension) is represented by a stratified film of about 20 multilayered nanosheets.

On other hand, based on the variation of the dark- and photo-currents of the Mo_2CT_x thin films (at 660 nm) as a function of different film thicknesses (**Figure S17**), we know that a thickness, Δx, of 2 μm is enough to reach a value larger than 95% of the collectable photocurrent. Then by assuming that the nanosheets stratification (like other statistically significant ensembles) is characterized by an absorbance proportional to the cross-section length subjected to light penetration; i.e. when the intensity $I = I_0 e^{-\alpha \Delta x}$, we can evaluate the

specific absorption per layer, which is a 100 nm in thickness. Note that the increase in thickness above 2 μm does not correspond to a significant increase in the photocurrent. This model gives an absorption length scale, α, about 1.5 μm, hence an absorption per nanosheet (ca. 100 nm thick) of about 14%. It also provides an estimation of the number of monolayers involved in the whole photoconversion process; which is about two thousands.

Owing to the electron confinements and to the transversal size (thickness) of each multilayer cluster, this descriptive picture supports the idea of cooperative, tightly interacting, 2D plasmonic excitations stratified on each nanosheet and extending in the volume. Although each nanosheet has its own independent surface plasmon character due to their weak interlayer coupling,[9] they contribute to the SP character of the whole volume (thickness). Coupling with light and dephasing of SPs on nanostructured plasmonic devices (composed of different thicknesses of stacked nanosheets) has important implications on the energy distribution of the generated hot electrons and their lifetime. This leads to a response outperforming that of photoelectron-based semiconductor devices. Though Mo_2CT_x certainly cannot be considered as a conventional plasmonic material, the performed studies on noble metals platelets and on the plasmonic coupling of nearby nanostructures have to retain some correspondence and prediction ability.[32]

STEM/EELS characterization

Figures 3a and **S23-S26** demonstarte the EELS fitted intesnity maps of various SP modes supported by multiple Mo_2CT_x nanosheets with different shapes, sizes and thicknesses. As illustrated below, each nanosheet is sustaining a distinct set of multipolar longitudinal SP modes at different geometrical-dependent resonance energies. In contrast, regardless of their geometrical aspects, all the nanosheets exhibit an invarient transversal SP mode at 2.45 eV (e.g. **Figures 3a** and **S23**), which is characteristic of the material itself and solely depends on its free carrier concentration.[9] Likewise, **Figures 27** and **28** display the EELS fitted intesnity maps of the longitudinal and transversal SP modes supported by $Ti_3C_2T_x$ nanosheets. Analogous to Mo_2CT_x, the Ti-based MXene nanosheets are also sustaining distinct set of multipolar longitudinal SP modes that strongly depend on the geometrical aspects of each nanosheet. They alos demonstrate an invariant transversal SP mode at 1.7 eV, charactertstic of $Ti_3C_2T_x$.[9]

In princinple, longitudinal SP modes arise from the free electron oscillation along the main axes of the nanosheets. Generally, they are much stronger, lower in energy and highly size-dependent.[33-37] Analogous multipolar longitudinal modes have been observed in other metallic and 2D nanostructures including $Ti_3C_2T_x$ MXene.[9,37-51] Contrarily, a transversal SP mode, which is excited when the incident electric field is perpendicular to the main axes of the nanosheets, is higher in energy and size-independent.[34] Transversal modes in the visible range were also reported for other 2D materials such as $Ti_3C_2T_x$ MXene and graphene.[9,52]

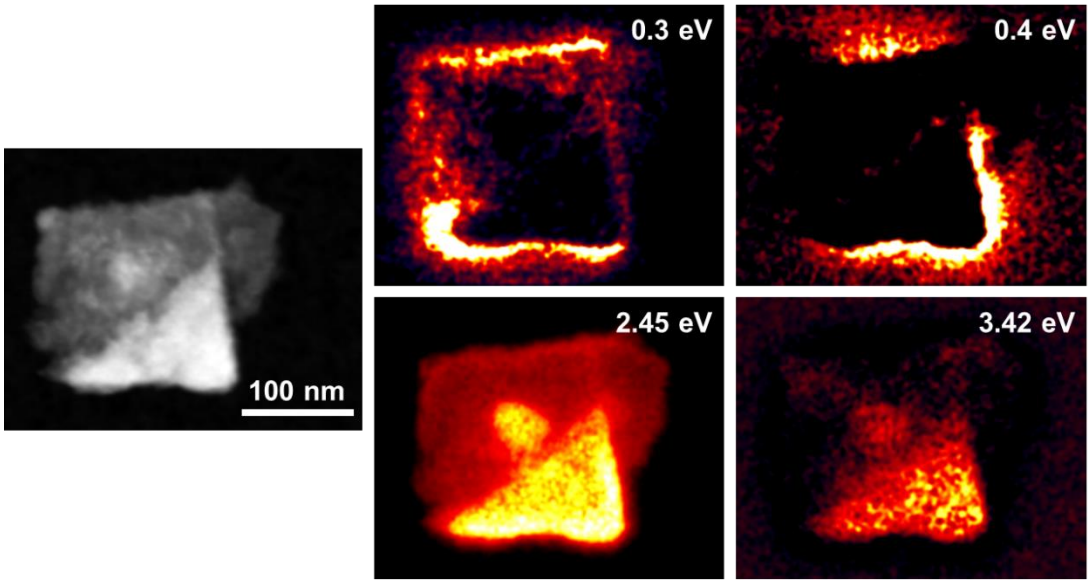

Figure S23. ADF-STEM micrograph of a rectangular Mo_2CT_x nanosheet (ca. 46 nm ± 1 at the bottom-right part) along with the corresponding EELS fitted intensity maps of the supported SP modes and IBT. Two longitudinal SP modes were detected at 0.3 and 0.4 eV. The transversal mode and IBT were detected at 2.45 and 3.42 eV, respectively.

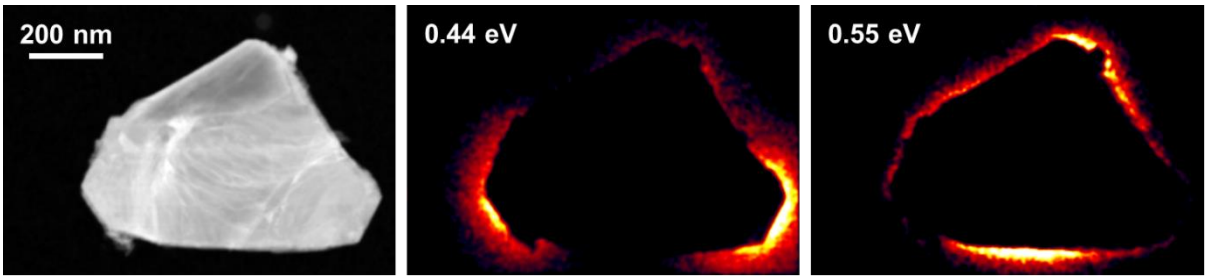

Figure S24. ADF-STEM micrograph of a truncated triangular Mo_2CT_x nanosheet (ca. 126 nm ± 1) along with the corresponding EELS fitted intensity maps of two longitudinal SP modes detected at 0.44 and 0.55 eV. The geometrical complexity prevented the assignment of the detected spatial distributions to specific modes. Transverse mode and IBT were not detected because of the large thickness.

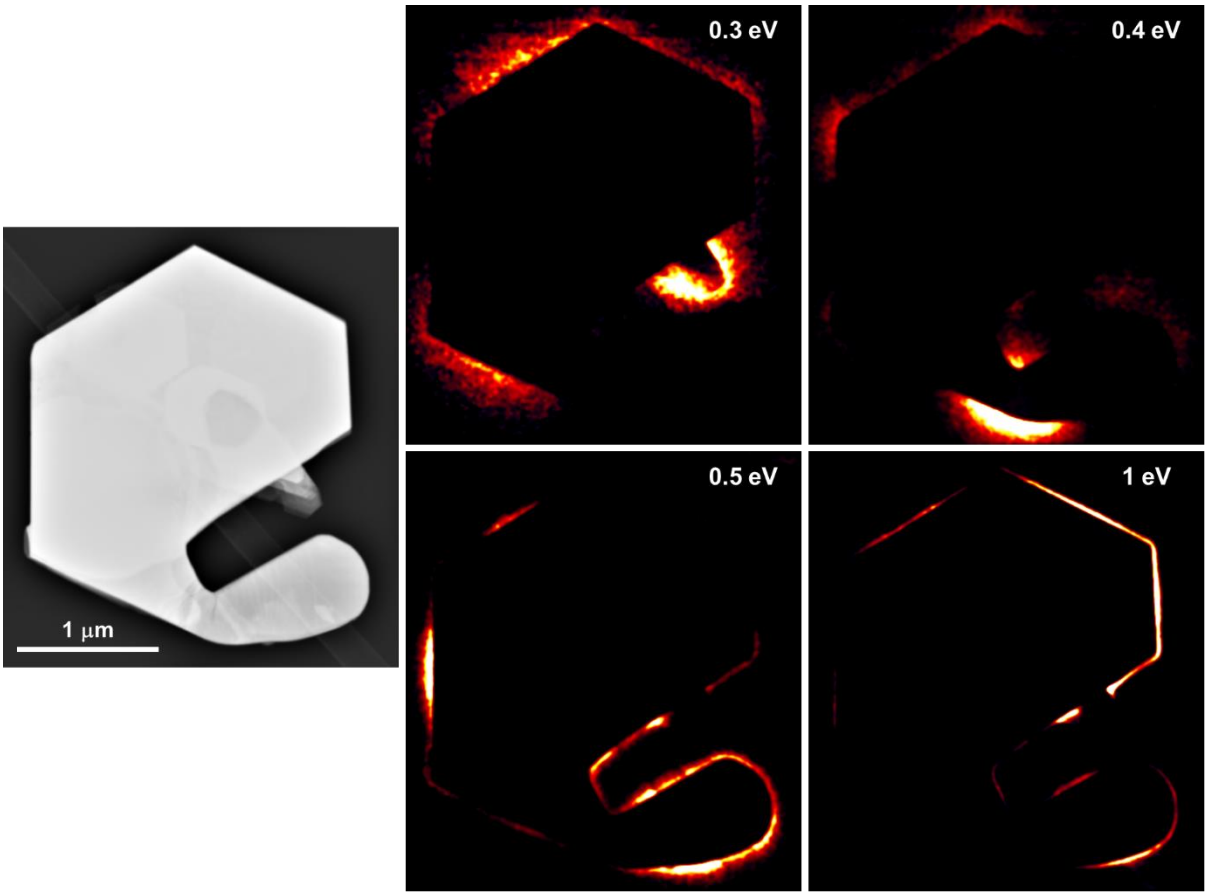

Figure S25. ADF-STEM micrograph of a complex hexagonal Mo_2CT_x nanosheet (ca. 142 nm ± 1) along with the corresponding EELS fitted intensity maps of four longitudinal SP modes detected at 0.3, 0.4, 0.5 and 1 eV. The geometrical complexity prevented the assignment of the detected spatial distributions to specific modes. Transverse mode and IBT were not detected because of the large thickness.

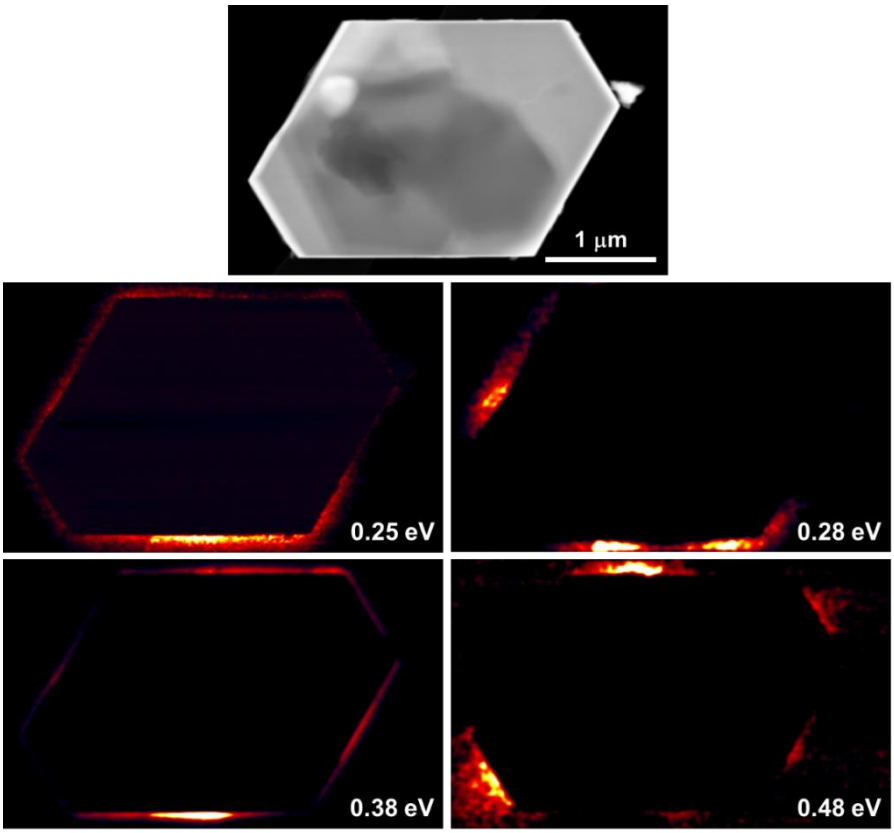

Figure S26. ADF-STEM micrograph of a hexagonal Mo_2CT_x nanosheet (ca. 148 nm ± 1) along with the corresponding EELS fitted intensity maps of five longitudinal SP modes detected at 0.25, 0.28, 0.38 and 0.48 eV. The geometrical complexity prevented the assignment of the detected spatial distributions to specific modes. Transverse mode and IBT were not detected because of the large thickness.

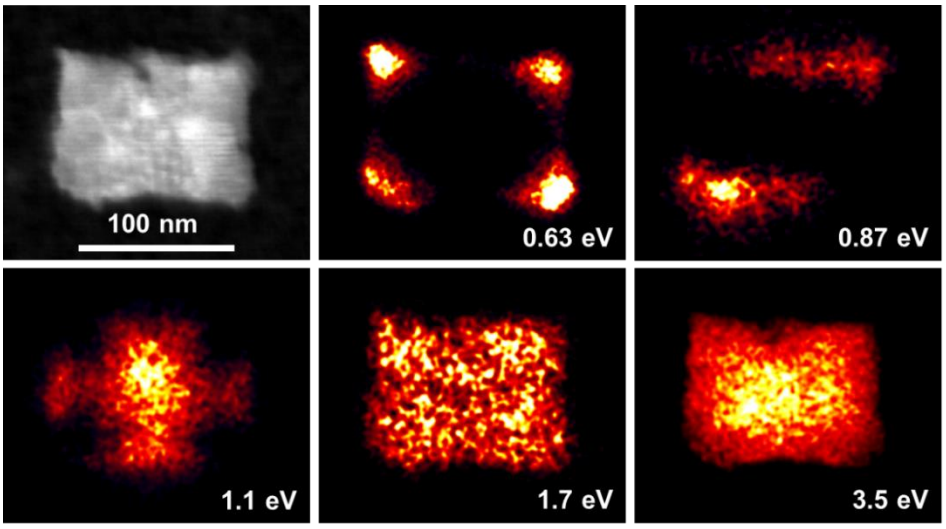

Figure S27. ADF-STEM micrograph of a square-like $Ti_3C_2T_x$ nanosheet (ca. 10.5 nm) along with the corresponding EELS fitted intensity maps of the supported longitudinal SP modes, *i.e.*, dipole, quadrupole and breathing at 0.63, 0.87 and 1.1 eV, respectively. The transversal mode and IBT were detected at 1.7 and 3.5 eV, respectively.

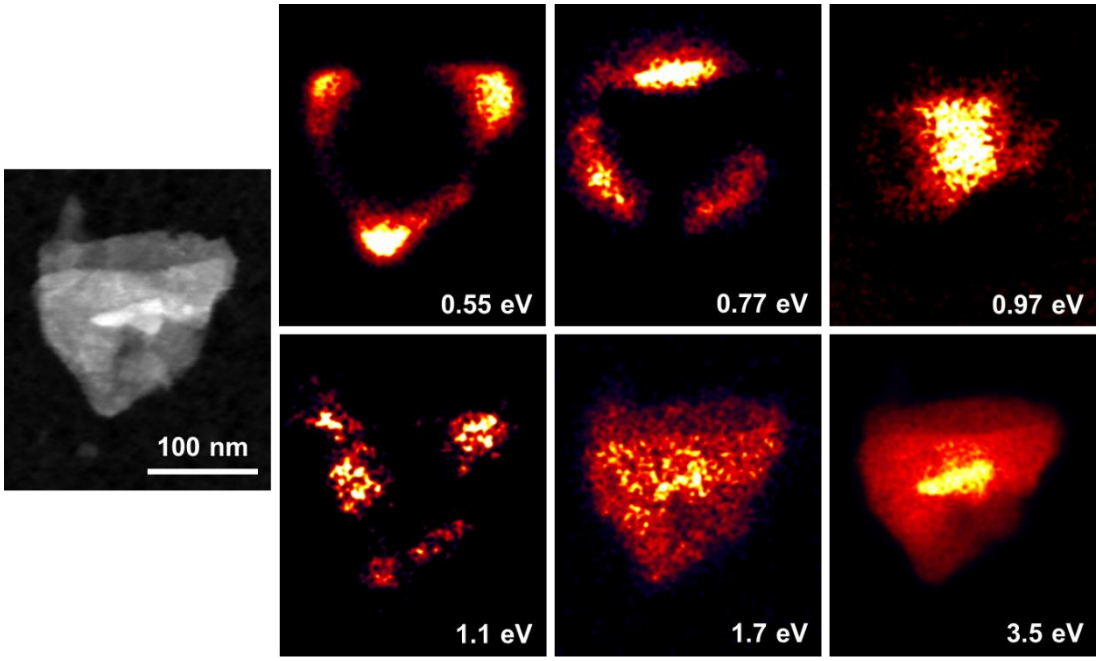

Figure S28. ADF-STEM micrograph of a triangular $Ti_3C_2T_x$ nanosheet (ca. 9 nm) along with the corresponding EELS fitted intensity maps of the supported longitudinal SP modes, *i.e.*, dipole, quadrupole, breathing and a high order central mode at 0.55, 0.77, 0.97 and 1.1 eV, respectively. The transversal mode and IBT were detected at 1.7 and 3.5 eV, respectively.

Ellipsometry

We conducted spectroscopic ellipsometric measurements to obtain the real and imaginary components of the permittivity of Mo_2CT_x thin films (**Figure S29**). The ellipsometry data was fitted using a Drude model and a set of imaginary harmonic oscillators, as summarized in **Table S3**. To our knowledge, such information have not been reported before.

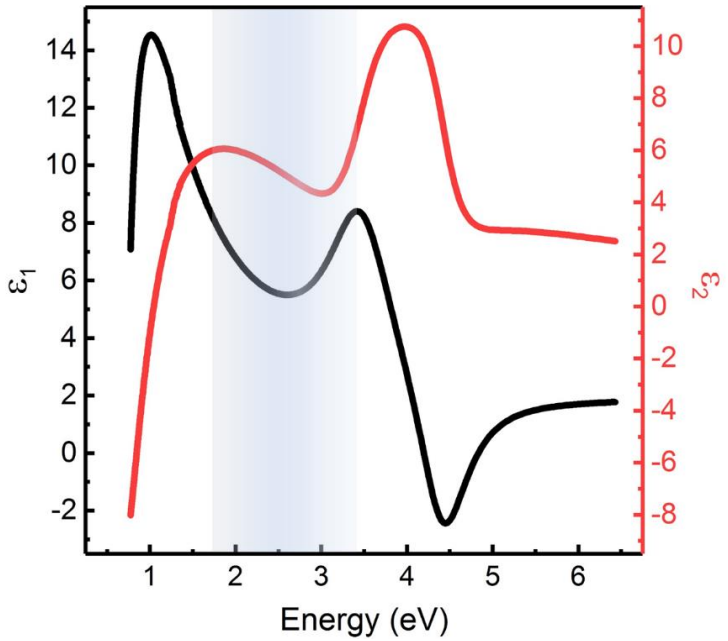

Figure S29. Experimentally measured permittivity of ca 7.5 nm Mo_2CT_x film as a function of incident photon energy, showing the real component (black) and the imaginary component (red) as modeled from spectroscopic ellipsometry data. The shaded part highlights the energy window of the transversal SP mode supported by Mo_2CT_x nanosheets.

Table S3. The fitting parameters of the optical response of a ca. 7.5 nm thick Mo_2CT_x film as derived from spectroscopic ellipsometry measurements.

Drude: $\boldsymbol{\varepsilon = \frac{-\hbar^2}{\varepsilon_0 \rho_n (\tau_n . E^2 + i\hbar E)}}$				
ρ (Ω.cm)		τ (fs)		
0.00021521		0.0935		
Harmonic Oscillators: $\boldsymbol{\varepsilon = \frac{[Amp_n + i(Amp_n)]Br_n}{2}\left(\frac{1}{E_n - E - i\frac{Br_n}{2}} + \frac{1}{E_n + E - i\frac{Br_n}{2}}\right)}$				
	Amp_n	$i(Amp_n)$	E_n (eV)	Br_n (eV)
1st Harmonic	0.644651	-5.6254	3.979	0.5757
2nd Harmonic	956.825333	-709.7536	0.343	0.1622
3rd Harmonic	0.422865	6.0103	0.7836	3.197

In contrast to conventional plasmonic metals, **Figure S29** shows that the dielectric constant of the Mo_2CT_x film (ca. 7.5 nm thick) remains to be positive in a wide range, in spite of the plasmonic behavior illustrated by EELS (**Figures 3a** and **S23-S26**).

To correlate between this measured positive permittivity dispersion and our explanation of the induced photocurrent based on SP-assisted hot electron generation, we introduce two concurrent, yet different, arguments. One is about the nature of SPs and the constituting equations,[53,54] while the second argument relies on previous experimental results of "classical" plasmonic nanostructures and thin films as demonstrated in the literature.[55,56]

First argument: When we deduced the existence of SPs in Mo_2CT_x, and thought of relying on them to explain our device performance, we had to verify the validity of the hypothesis used to derive field equations as well as dispersion relations, to assure their applicability to the considered case. The formal well-known relation between frequency, wave vector of the surface plasmon polariton (SPP), and the dielectric constants at the interface: $K_{SP}^2(\omega) = \frac{\omega^2}{c^2}\frac{\epsilon_1\epsilon_2}{\epsilon_1+\epsilon_2}$ (**Eq. 1**), allows for the possibility to derive different wave equations for the propagating SP modes along with their dispersion relations. Either by simply considering the lossy or lossless nature of the SP propagation (or the one of a standing resonance), one would have at least three ways to describe the plasmonic material in terms of SPs and dispersion relation.

In the simple and the most common case; i.e. assumption of no losses in the Drude model hypothesis, two conditions: $\epsilon_1\epsilon_2 < 0$ and $\epsilon_1 + \epsilon_2 < 0$, are needed to imply the existence of SPs characterized by a real K_{SP}, which offers a long propagation character to the collective excitation, well beyond the single electron mean free path. This is the standard way to model SPPs. It also gives rise to the known dispersion relation associated with SPPs in noble metals that opens to the main nanoplasmonic results, the strong nanofocusing (field enhancement) and the boost of the local density of states, leading to the energy confinement in hot spots.[57,58]

In a general case (like ours), SPs can be highly dissipative excitations,[9,51], where the peak line width of their EELS signal results is directly proportional to the induced damping.[9,51,59] Thus, the SPs assume a localized character due to the short propagation prior to damping, which mainly occurs during the process of SP-assisted hot-electron generation. The propagation distance, however, has to be always compared with the nanoscale size of the plasmonic material (i.e. a cluster of nanosheets in our case, where every nanosheet is extending for hundreds of nanometers). If the dephasing process of the SP happens in the nearby of the edges or at the edges of the nanosheets, the energized electrons can then be collected efficiently.[29,30]

In the above dissipative case, the dispersion relation still can be obtained by solving the aforementioned **Eq. 1**, by either using combination of a real frequency and an imaginary wave vector, or a combination of a real wave vector and an imaginary frequency. Note that the shape of the dispersion relation would straightly depend on the chosen combination. As a consequence, the SP wave equations will be different and the previously mentioned dielectric constraints will no longer be required. While one dispersion relation have an asymptote for very large values of K (obtained by plotting the points from a spectrum at fixed angle in a reflectivity experiment), the other is characterized by a K_{max} value and is represented by a backbending curve (obtained by plotting the position of the reflectivity dips as function of the angle of incidence at fixed frequency).[60] The first combination (with complex wave vectors) is properly used to represent a SP as stationary monochromatic fields excited in a finite area, while the second (with complex frequencies) is well adapted to fields excited by pulses.

This analogy remarks that, in general, when we have lossy medium (like in our case), the condition for propagating SPs is not implicit in the condition $\epsilon_1\epsilon_2 < 0$ and $\epsilon_1 + \epsilon_2 < 0$. Meaning that both of the above dispersion relations deriving the k_{SP}, can also have $\epsilon_{plasmonic\ material} > 0$.

Second argument: In previously reported experimental results, the effective optical properties of conventional plasmonic nanostructures were demonstrated to strongly depend on the filling fraction (packing density) of the nanoparticles constituting the film,[55] and on the thin film thickness.[56] In the latter work, for instance, at a thickness of ca. 4.7 nm, the dielectric constant ($\varepsilon=n^2-k^2$) of silver thin films behaved completely different and stayed positive in a wide spectral range.

Building upon the implications of these two works, it is no longer possible to attribute optical properties established with effective medium theories to plasmonic nanocomposites. (However, effective medium theories can still describe a plasmonic nanostructure with a filling fraction close to the percolation threshold.) Moreover, the effective optical constants of ultrathin plasmonic metal films clearly depend on the thickness, unlike the bulk optical constants, and thus can be described precisely with the use of an effective thickness. Hence, in our case, it is acceptable for Mo_2CT_x films to demonstrate a positive permittivity dispersion at low thicknesses (ca. 7.5 nm), while maintaining its plasmonic character.

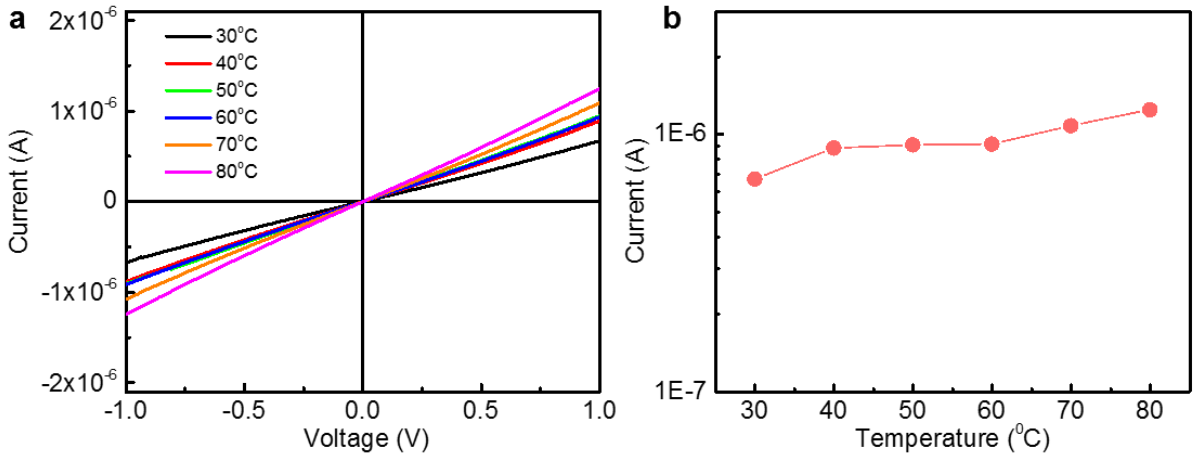

Figure S30. Dark current variation of Mo_2CT_x thin film as a function of device temperature with a fixed bias voltage of -1 V. The very small change in current as function of temperature shows that both photothermoelectric and bolometric effects are marginal.

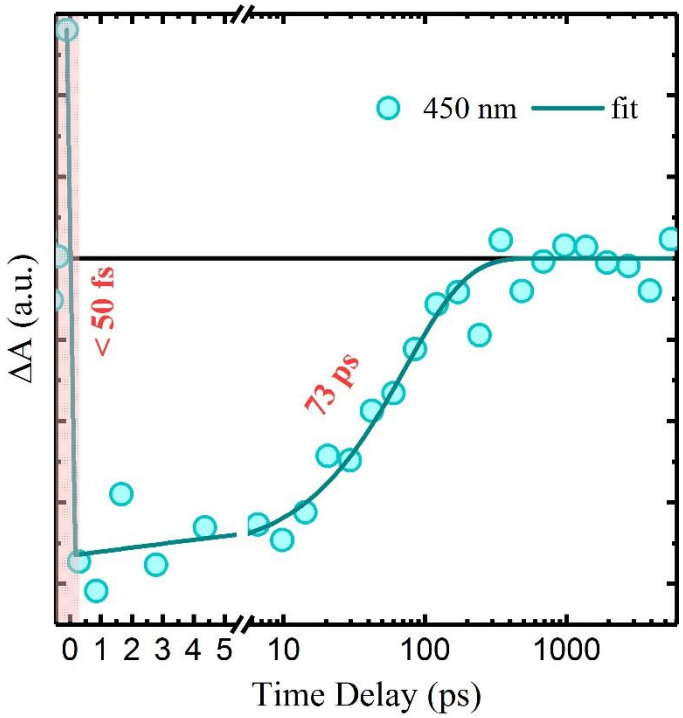

Figure S31. Kinetic traces of $Ti_3C_2T_x$ extracted at 450 nm. The data were performed under excitation wavelength of 330 nm. Two lifetime components are needed for the best fit; one rising component for the plasmon-excitation process of ca. 50 fs, and another component of ca. 70 ps for the recombination process of the plasmon-induced excited carriers.

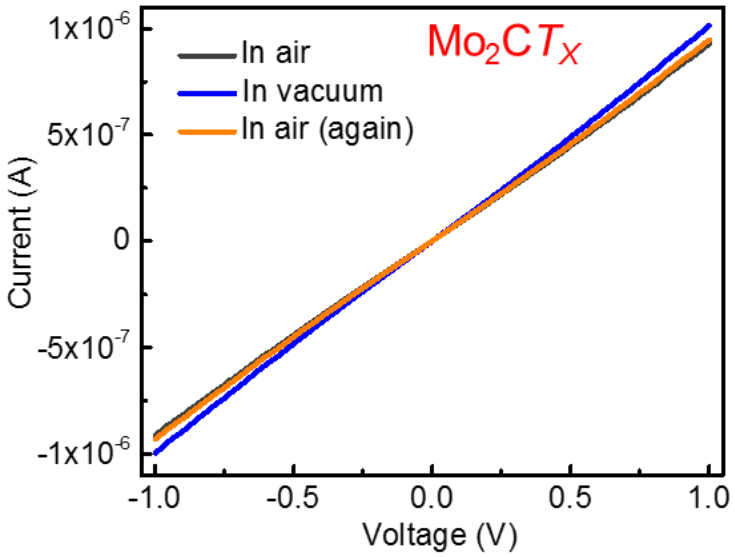

Figure S32. Current-voltage *I-V* characteristics of a Mo_2CT_x thin film without light illumination measured in air (black), under vacuum (blue) and in air again (red) under a bias voltage of ±1 V. No obvious difference was observed.

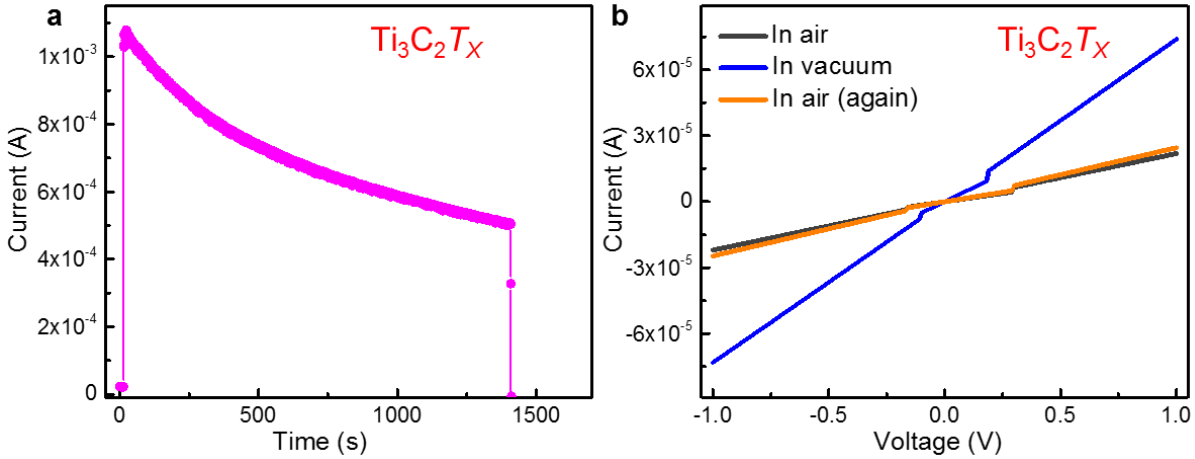

Figure S33. a, Photostability of the $Ti_3C_2T_x$ thin film photodetector devices under continuous illumination of 660 nm light in ambient conditions. **b**, Current-voltage *I-V* characteristics of a $Ti_3C_2T_x$ thin film without light illumination measured in air (black), under vacuum (blue) and in air again (red) under a bias voltage of ±1 V. Notice the recovery in the *I-V* characteristics once the film is re-exposed to air.

Table S4. Comparison of the key parameters of Mo_2CT_x MXene to the reported 2D material based photodetectors.

Material	***Process***	***Device architecture***	***Spectral Range***	***Responsivity (A W^{-1})***	***Detectivity (Jones)***	***Refer--ence***
Mo_2CT_x MXene	Solution Synthesis	2 terminal Photoconductor	Visible	9	$5x10^{11}$	This work
Graphene	Mechanical Exfoliation	3 terminal FET	Visible	$5x10^{-4}$	No data	61
	Mechanical Exfoliation	3 terminal FET	Visible	$1x10^{-3}$	No data	62
	CVD	3 terminal FET	Visible	$5x10^{-4}$	No data	63
Graphene-Plasmonic nanoparticles	CVD	3 terminal FET	Visible	$6.1x10^{-3}$	No data	64
Reduced Graphene Oxide	Solution Synthesis	2 terminal Photoconductor	NIR	$4x10^{-3}$	No data	65
	Solution Synthesis	2 terminal Photoconductor	UV	$5.6x10^{-2}$	No data	66
Graphene Nano-ribbons	Solution Synthesis	2 terminal Photoconductor	NIR	1	No data	65
MoS_2	Mechanical Exfoliation	3 terminal FET	Visible	$7.5x10^{-3}$	No data	67
	Mechanical Exfoliation	3 terminal FET	Visible	880	No data	68
	CVD	2 terminal Photoconductor	Visible	0.57	No data	69

Cont…

	Liquid Phase Exfoliation	2 terminal Photoconductor	Visible	No data	~$2x10^{11}$	70
	Liquid Phase Exfoliation	2 terminal Photoconductor	White light	~10^{-4}	No data	71
	Liquid Phase Exfoliation	2 terminal Photoconductor	Visible	0.7	~$2x10^{11}$	72
WS_2	CVD	2 terminal Photoconductor	Visible	$9.5x10^{-5}$	No data	73
	Magnetron Sputtering	2 terminal Photoconductor	UV	53.3	$1.22x10^{11}$	74
	Liquid Phase Exfoliation	2 terminal Photoconductor	Visible	$4.5x10^{-5}$	No data	75
$MoSe_2$	CVD	2 terminal Photoconductor	Visible	$1.3x10^{-2}$	No data	76
	CVD	3 terminal FET	Visible	93.7	No data	77
	Liquid Phase Exfoliation	2 terminal Photoconductor	NIR	16	$1x10^{12}$	70
Black Phosphorous	Mechanical Exfoliation	3 terminal FET	Visible	4.8 $x10^{-3}$	No data	78
	Mechanical Exfoliation	3 terminal FET	NIR	8.5	No data	79
	Mechanical Exfoliation	3 terminal FET	UV	~$9x10^{4}$	~$3x10^{13}$	80

Cont…

	Liquid Phase Exfoliation	2 terminal Photoconductor	UV	$7.1x10^{-3}$	$\sim1x10^{11}$	72
GaS	CVD	2 terminal Photoconductor	UV	19.2	$1x10^{14}$	81
	Mechanical Exfoliation	2 terminal Photoconductor	Visible	64.43	No data	82
	Solution Synthesis	2 terminal Photoconductor	UV	173	$1.74x10^{13}$	83
GaSe	Mechanical Exfoliation	2 terminal Photoconductor	UV	2.8	No data	84
	Solution Synthesis	2 terminal Photoconductor	UV	870	$1.12x10^{13}$	83
$SnSe_2$	CVD	2 terminal Photoconductor	Visible	$1.3x10^{3}$	$1\ x10^{10}$	85
	CVD	2 terminal Photoconductor	NIR	1.9	No data	86
InSe	Liquid Phase Exfoliation	2 terminal Photoconductor	White Light	$5x10^{-6}$	No data	87
$NiPS_3$	CVD	2 terminal Photoconductor	UV	$1.26x10^{-1}$	$1.22\ x10^{12}$	88
Tellurium nanosheets	Solution Synthesis	2 terminal Photoconductor	NIR	13	$2\ x10^{9}$	89
$PtSe_2$ nanosheet thin film	CVD	2 terminal Photoconductor	NIR	0.5	No data	90

References

[1] J. Halim, S. Kota, M. R. Lukatskaya, M. Naguib, M.-Q. Zhao, E. J. Moon, J. Pitock, J. Nanda, S. J. May, Y. Gogotsi, M. W. Barsoum, *Adv. Funct. Mater.* **2016**, *26*, 3118.

[2] M. Naguib, M. Kurtoglu, V. Presser, J. Lu, J. Niu, M. Heon, L. Hultman, Y. Gogotsi, M. W. Barsoum, *Adv. Mater.* **2011**, *23*, 4248.

[3] M. Naguib, J. Halim, J. Lu, K. M. Cook, L. Hultman, Y. Gogotsi, M. W. Barsoum, *J. Am. Chem. Soc.* **2013**, *135*, 15966.

[4] R. B. Rakhi, B. Ahmed, M. N. Hedhili, D. H. Anjum, H. N. Alshareef, *Chem.Mater.* **2015**, *27*, 5314.

[5] S. M. Aly, M. R. Parida, E. Alarousu, O. F. Mohammed, *Chem. Commun.* **2014**, *50*, 10452.

[6] A. A. Govyadinov, A. Konečná, A. Chuvilin, S. Vélez, I. Dolado, A. Y. Nikitin, S. Lopatin, F. Casanova, L. E. Hueso, J. Aizpurua, R. Hillenbrand, *Nat. Commun.* **2017**, *8*, 95.

[7] S. Lopatin, B. Cheng, W.-T. Liu, M.-L. Tsai, J.-H. He, A. Chuvilin, Ultramicroscopy **2018**, *184*, 109.

[8] R.F. Egerton, *Electron energy-loss spectroscopy in the electron microscope. 3rd edn,* Springer, New York, **2011.**

[9] J. K. El-Demellawi, S. Lopatin, J. Yin, O. F. Mohammed, H. N. Alshareef, *ACS Nano* **2018**, *12*, 8485.

[10] J. Zhu, Y. Tang, C. Yang, F. Wang, M. Cao, *J. Electrochem. Soc.* **2016**, *163*, A785.

[11] Y. Dall'Agnese, M. R. Lukatskaya, K. M. Cook, P.-L. Taberna, Y. Gogotsi, P. Simon, *Electrochem. Commun.* **2014**, *48*, 118.

[12] J. Halim, K. M. Cook, M. Naguib, P. Eklund, Y. Gogotsi, J. Rosen, M. W. Barsoum, *Appl. Surf. Sci.* **2016**, *362*, 406.

[13] M. C. Biesinger, L. W. M. Lau, A. R. Gerson, R. S. C. Smart, *Appl. Surf. Sci.* **2010**, 257, 887.

[14] J. Halim, M. R. Lukatskaya, K. M. Cook, J. Lu, C. R. Smith, L.-Å. Näslund, S. J. May, L.

Hultman, Y. Gogotsi, P. Eklund, M. W. Barsoum, *Chem. Mater.* **2014**, *26*, 2374.

[15] A. Daccà, G. Gemme, L. Mattera, R. Parodi, *Appl. Surf. Sci.* **1998**, *126*, 219.

[16] M. Naguib, J. Halim, J. Lu, K. M. Cook, L. Hultman, Y. Gogotsi, M. W. Barsoum, *J. Am. Chem. Soc.* **2013**, *135*, 15966.

[17] J-G. Choi, *Appl. Surf. Sci.* **1999**, *148*, 64.

[18] M. Hassan, R. S. Rawat, P. Lee, S. M. Hassan, A. Qayyum, R. Ahmad, G. Murtaza, M. Zakaullah, *Appl. Phy. A* **2008**, *90*, 669.

[19] B. H. Q. Dang, M. Rahman, D. MacElroy, D. P. Dowling, *Surf. Coat. Tech.* **2012**, *206*, 4113.

[20] M. M. Ottakam Thotiyl, S. A. Freunberger, Z. Peng, Y. Chen, Z. Liu, P. G. Bruce, *Nat. Mater.* **2013**, *12*, 1050.

[21] S. Zhang, Y. Q. Fu, X. L. Bui, H. J. Du, *Int. J.Nanosci.* **2004**, *03*, 797.

[22] G. Liu, C. Han, M. Pelaez, D. Zhu, S. Liao, V. Likodimos, N. Ioannidis, A. G. Kontos, P. Falaras, P. S. M. Dunlop, J. A. Byrne, D. D. Dionysiou, *Nanotechnol.* **2012**, *23*, 294003.

[23] T. Livneh, T. L. Haslett, M. Moskovits, *Phy. Rev. B* **2002**, *66*, 195110.

[24] H. Kim, B. Anasori, Y. Gogotsi, H. N. Alshareef, *Chem. Mater.* **2017**, *29*, 6472.

[25] U. Yorulmaz, A. Özden, N. K. Perkgöz, F. Ay, C. Sevik, *Nanotechnology* **2016**, *27*, 335702.

[26] M. Khazaei, M. Arai, T. Sasaki, C.-Y. Chung, N. S. Venkataramanan, M. Estili, Y. Sakka, Y. Kawazoe, *Adv. Funct. Mater.* **2013**, *23*, 2185.

[27] M. Dieterle, G. Mestl, *Phys. Chem. Chem. Phys.* 2**002**, *4*, 822.

[28] M. Dieterle, G. Weinberg, G. Mestl, *Phys. Chem. Chem. Phys.* **2002**, *4*, 812.

[29] A. O. Govorov, H. Zhang, Y. K. Gun'ko, *J. Phys. Chem. C* **2013**, *117*, 16616.

[30] L. V. Besteiro, X.-T. Kong, Z. Wang, G. Hartland, A. O. Govorov, *ACS Photonics* **2017**, *4*, 2759.

[31] V. Mauchamp, M. Bugnet, E. P. Bellido, G. A. Botton, P. Moreau, D. Magne, M. Naguib,

T. Cabioc'h, M. W. Barsoum, *Phys. Rev. B* **2014**, *89*, 235428.

[32] M.-W. Chu, V. Myroshnychenko, C. H. Chen, J.-P. Deng, C.-Y. Mou, F. J. García de Abajo, *Nano Lett.* **2009**, *9*, 399.

[33] J. Nelayah, M. Kociak, O. Stéphan, N. Geuquet, L. Henrard, F. J. García de Abajo, I. Pastoriza-Santos, L. M. Liz-Marzán, C. Colliex, *Nano Lett.* **2010**, *10*, 902.

[34] N. Nehru, E. U. Donev, G. M. Huda, L. Yu, Y. Wei, J. T. Hastings, *Opt. Exp.* **2012**, *20*, 6905.

[35] A. A. Govyadinov, A. Konečná, A. Chuvilin, S. Vélez, I. Dolado, A. Y. Nikitin, S. Lopatin, F. Casanova, L. E. Hueso, J. Aizpurua, R. Hillenbrand, *Nat. Commun.* **2017**, *8*, 95.

[36] A. L. Koh, K. Bao, I. Khan, W. E. Smith, G. Kothleitner, P. Nordlander, S. A. Maier, D. W. McComb, *ACS Nano* **2009**, *3*, 3015.

[37] A. Losquin, L. F. Zagonel, V. Myroshnychenko, B. Rodríguez-González, M. Tencé, L. Scarabelli, J. Förstner, L. M. Liz-Marzán, F. J. García de Abajo, O. Stéphan, M. Kociak, *Nano Lett.* **2015**, *15*, 1229.

[38] J. Nelayah, M. Kociak, O. Stéphan, F. J. García de Abajo, M. Tencé, L. Henrard, D. Taverna, I. Pastoriza-Santos, L. M. Liz-Marzán, C. Colliex, *Nat. Phy.* **2007**, *3*, 348.

[39] L. Gu, W. Sigle, C. T. Koch, B. Ögüt, P. A. van Aken, N. Talebi, R. Vogelgesang, J. Mu, X. Wen, J. Mao, *Phy. Rev. B* **2011**, *83*, 195433.

[40] F. Huth, A. Chuvilin, M. Schnell, I. Amenabar, R. Krutokhvostov, S. Lopatin, R. Hillenbrand, *Nano Lett.* **2013**, *13*, 1065.

[41] L. H. Karlsson, J. Birch, J. Halim, M. W. Barsoum, P. O. Å. Persson, *Nano Lett.* **2015**, *15*, 4955.

[42] D. Rossouw, M. Couillard, J. Vickery, E. Kumacheva, G. A. Botton, *Nano Lett.* **2011**, *11*, 1499.

[43] S. Raza, S. Kadkhodazadeh, T. Christensen, M. Di Vece, M. Wubs, N. A. Mortensen, N. Stenger, *Nat. Commun.* **2015**, *6*, 8788.

[44] A. Campos, A. Arbouet, J. Martin, D. Gérard, J. Proust, J. Plain, M. Kociak, *ACS Photonics* **20**17, *4*, 1257.

[45] S. J. Barrow, D. Rossouw, A. M. Funston, G. A. Botton, P. Mulvaney, *Nano Lett.* **2014**, *14*, 3799.

[46] V. J. Keast, C. J. Walhout, T. Pedersen, N. Shahcheraghi, M. B. Cortie, D. R. G. Mitchell, *Plasmonics* **2016**, *11*, 1081.

[47] E. P. Bellido, A. Manjavacas, Y. Zhang, Y. Cao, P. Nordlander, G. A. Botton, *ACS Photonics* **2016**, *3*, 428.

[48] F.-P. Schmidt, H. Ditlbacher, U. Hohenester, A. Hohenau, F. Hofer, J. R. Krenn, *Nat. Commun.* **2014**, *5*, 3604.

[49] R. G. Hobbs, V. R. Manfrinato, Y. Yang, S. A. Goodman, L. Zhang, E. A. Stach, K. K. Berggren, *Nano Lett.* **2016**, *16*, 4149.

[50] F. P. Schmidt, H. Ditlbacher, F. Hofer, J. R. Krenn, U. Hohenester, *Nano Lett.* **2014**, *14*, 4810.

[51] M. Kociak, O. Stéphan, *Chem. Soc. Rev.* **2014**, *43*, 3865.

[52] A. N. Grigorenko, M. Polini, K. S. Novoselov, *Nat. Photonics* **2012**, *6*, 749.

[53] Stefan Enoch and Nicolas Bonod, *Plasmonics: from basic to advanced topics*, Springer, New York, **2012**

[54] A. Archambault, T. V. Teperik, F. Marquier, J. J. Greffet, *Phy. Rev. B* **2009**, *79*, 195414.

[55] C. Etrich, S. Fahr, M. K. Hedayati, F. Faupel, M. Elbahri, C. Rockstuhl, *Materials* **2014**, *7*, 727.

[56] J. Gong, R. Dai, Z. Wang, Z. Zhang, *Sci. Rep.* **2015**, *5*, 9279.

[57] A. Giugni, B. Torre, M. Allione, G. Das, Z. Wang, X. He, H. N. Alshareef, E. Di Fabrizio, *Adv. Opt. Mater.* **2017**, *5*, 1700195.

[58] A. Giugni, B. Torre, A. Toma, M. Francardi, M. Malerba, A. Alabastri, R. Proietti Zaccaria, M. I. Stockman, E. Di Fabrizio, *Nat. Nanotechnol.* **2013**, *8*, 845.

[59] Z. Zhu, Y. Zou, W. Hu, Y. Li, Y. Gu, B. Cao, N. Guo, L. Wang, J. Song, S. Zhang, H. Gu, H. Zeng, *Adv. Funct. Mater.* **2016**, *26*, 1793.

[60] E. T. Arakawa, M. W. Williams, R. N. Hamm, R. H. Ritchie, *Phy. Rev. Let.* **1973**, *31*, 1127.

[61] F. Xia, T. Mueller, Y.-m. Lin, A. Valdes-Garcia, P. Avouris, *Nat. Nanotechnol.* **2009**, *4*, 839.

[62] F. Xia, T. Mueller, R. Golizadeh-Mojarad, M. Freitag, Y.-m. Lin, J. Tsang, V. Perebeinos, P. Avouris, *Nano Lett.* **2009**, *9*, 1039.

[63] V. Patil, A. Capone, S. Strauf, E.-H. Yang, *Sci. Rep.* **2013**, *3*, 2791.

[64] Y. Liu, R. Cheng, L. Liao, H. Zhou, J. Bai, G. Liu, L. Liu, Y. Huang, X. Duan, *Nat. Commun.* **2011**, *2*, 579.

[65] B. Chitara, L. S. Panchakarla, S. B. Krupanidhi, C. N. R. Rao, *Adv. Mater.* **2011**, *23*, 5419.

[66] Y. Cao, H. Yang, Y. Zhao, Y. Zhang, T. Ren, B. Jin, J. He, J.-L. Sun, *ACS Photonics* **2017**, *4*, 2797.

[67] Z. Yin, H. Li, H. Li, L. Jiang, Y. Shi, Y. Sun, G. Lu, Q. Zhang, X. Chen, H. Zhang, *ACS Nano* **2012**, 6, 74.

[68] O. Lopez-Sanchez, D. Lembke, M. Kayci, A. Radenovic, A. Kis, *Nat. Nanotechnol.* **2013**, *8*, 497.

[69] D.-S. Tsai, K.-K. Liu, D.-H. Lien, M.-L. Tsai, C.-F. Kang, C.-A. Lin, L.-J. Li, J.-H. He, *ACS Nano* **2013**, *7*, 3905.

[70] D. B. Velusamy, R. H. Kim, S. Cha, J. Huh, R. Khazaeinezhad, S. H. Kassani, G. Song, S. M. Cho, S. H. Cho, I. Hwang, J. Lee, K. Oh, H. Choi, C. Park, *Nat. Commun.* **2015**, *6*, 8063.

[71] G. Cunningham, U. Khan, C. Backes, D. Hanlon, D. McCloskey, J. F. Donegan, J. N. Coleman, *J. Mater. Chem. C* **2013**, *1*, 6899.

[72] D. B. Velusamy, M. A. Haque, M. R. Parida, F. Zhang, T. Wu, O. F. Mohammed, H. N. Alshareef, *Adv. Funct. Mater.* **2017**, *27*, 1605554.

[73] N. Perea-López, A. L. Elías, A. Berkdemir, A. Castro-Beltran, H. R. Gutiérrez, S. Feng, R. Lv, T. Hayashi, F. López-Urías, S. Ghosh, B. Muchharla, S. Talapatra, H. Terrones, M. Terrones,

Adv. Funct. Mater. **2013**, *23*, 5511.

[74] L. Zeng, L. Tao, C. Tang, B. Zhou, H. Long, Y. Chai, S. P. Lau, Y. H. Tsang, *Sci. Rep.* **2016**, *6*, 20343.

[75] F. Withers, H. Yang, L. Britnell, A. P. Rooney, E. Lewis, A. Felten, C. R. Woods, V. Sanchez Romaguera, T. Georgiou, A. Eckmann, Y. J. Kim, S. G. Yeates, S. J. Haigh, A. K. Geim, K. S. Novoselov, C. Casiraghi, *Nano Lett.* **2014**, *14*, 3987.

[76] J. Xia, X. Huang, L.-Z. Liu, M. Wang, L. Wang, B. Huang, D.-D. Zhu, J.-J. Li, C.-Z. Gu, X.-M. Meng, *Nanoscale* **2014**, *6*, 8949.

[77] C. Jung, S. M. Kim, H. Moon, G. Han, J. Kwon, Y. K. Hong, I. Omkaram, Y. Yoon, S. Kim, J. Park, *Sci. Rep.* **2015**, *5*, 15313.

[78] M. Buscema, D. J. Groenendijk, S. I. Blanter, G. A. Steele, H. S. J. van der Zant, A. Castellanos-Gomez, *Nano Lett.* **2014**, *14*, 3347.

[79] L. Huang, W. C. Tan, L. Wang, B. Dong, C. Lee, K.-W. Ang, *ACS Appl. Mater. Interfaces* **2017**, *9*, 36130.

[80] J. Wu, G. K. W. Koon, D. Xiang, C. Han, C. T. Toh, E. S. Kulkarni, I. Verzhbitskiy, A. Carvalho, A. S. Rodin, S. P. Koenig, G. Eda, W. Chen, A. H. C. Neto, B. Özyilmaz, *ACS Nano* **2015**, *9*, 8070.

[81] P. Hu, L. Wang, M. Yoon, J. Zhang, W. Feng, X. Wang, Z. Wen, J. C. Idrobo, Y. Miyamoto, D. B. Geohegan, K. Xiao, in *Nano Lett.* **2013**, *13*, 1649.

[82] S. Yang, Y. Li, X. Wang, N. Huo, J.-B. Xia, S.-S. Li, J. Li, *Nanoscale* **2014**, *6*, 2582.

[83] P. Ramasamy, D. Kwak, D.-H. Lim, H.-S. Ra, J.-S. Lee *J. Mater. Chem. C* **2016**, *4*, 479.

[84] P. Hu, Z. Wen, L. Wang, P. Tan, K. Xiao, in *ACS Nano*, **2012**, *6*, 5988.

[85] X. Zhou, L. Gan, W. Tian, Q. Zhang, S. Jin, H. Li, Y. Bando, D. Golberg, T. Zhai, *Adv. Mater.* **2015**, *27*, 8035.

[86] Y. Huang, K. Xu, Z. Wang, T. A. Shifa, Q. Wang, F. Wang, C. Jiang, J. He, *Nanoscale* **2015**, *7*, 17375.

[87] Z. Li, H. Qiao, Z. Guo, X. Ren, Z. Huang, X. Qi, S. C. Dhanabalan, J. S. Ponraj, D. Zhang, J. Li, J. Zhao, J. Zhong, H. Zhang, *Adv. Funct. Mater.* **2018**, *28*, 1705237.

[88] J. Chu, F. Wang, L. Yin, L. Lei, C. Yan, F. Wang, Y. Wen, Z. Wang, C. Jiang, L. Feng, J. Xiong, Y. Li, J. He, *Adv. Funct. Mater.* **2017**, *27*, 1701342.

[89] M. Amani, C. Tan, G. Zhang, C. Zhao, J. Bullock, X. Song, H. Kim, V. R. Shrestha, Y. Gao, K. B. Crozier, M. Scott, A. Javey, in *ACS Nano*, **2018**, *12*, 7253.

[90] C. Yim, N. McEvoy, S. Riazimehr, D. S. Schneider, F. Gity, S. Monaghan, P. K. Hurley, M. C. Lemme, G. S. Duesberg, *Nano Lett.* **2018**, *18*, 1794.